Journal of the Mechanics and Physics of Solids, (2014), 64, 316-337.
DOI: http://dx.doi.org/10.1016/j.jmps.2013.11.006

Dynamic necking in materials with strain induced martensitic transformation

R. Zaera, J.A. Rodríguez-Martínez, G. Vadillo, J. Fernández-Sáez*

Department of Continuum Mechanics and Structural Analysis, University Carlos III of Madrid, Avda. de la Universidad, 30, 28911 Leganés, Madrid, Spain

*Corresponding author. Tel.: +34 916249964; fax: +34 916249430. *E-mail address:* ppfer@ing.uc3m.es (J. Fernández-Sáez).

Abstract: This work investigates the interplay between inertia and strain induced martensitic transformation (SIMT) on necking inception and energy absorption in dynamically stretched cylindrical rods. For that task a linear stability technique, derived within a quasi-1D framework and specifically accounting for SIMT, has been developed. Likewise, finite element simulations have been performed, using a specific constitutive equation to consider SIMT. Stability analysis and numerical simulations demonstrate that, at high strain rates, inertia may take the dominant role in stabilizing the material, on top of the transformation hardening effects. Furthermore, under certain loading conditions the martensitic transformation may penalize either ductility or energy absorption capacity.

Keywords: Martensitic transformation, Linear stability analysis, Numerical simulation, Ductility, Energy absorption

1. Introduction

Designers are concerned about potential collision events in car frameworks, pressure vessels and pipelines, ship hulls and many other crashworthiness and high-speed impact safety situations throughout engineering. In these systems, dedicated structural elements are employed and they are designed to deform following a specific pattern and to absorb energy. Thus, the knowledge of the energy absorption behavior is of importance for shape design and material selection in structures subjected to accidental impact and collision. Many studies have been published on the behavior of energy-absorbers through the inelastic response of the material (Hetherington, 1996; Jones, 1997; Jones et al., 2001; Lu and Yu, 2003; Dean et al., 2006; Rusinek et al., 2008; Rodríguez-Martínez et al., 2012). Analysis and design methods for energy-absorbers are different from standard structural design techniques, since they have to sustain strong impact loads and their deformation involves large geometric changes. Depending on the class of dynamic load applied to the system, different structural typologies and materials may be used. However, most energy absorbers are usually made up of materials that are (i) capable of keeping a high value of the stress upon deformation, and (ii) able to show a large value of strain at failure ε_f, the second requirement being strongly dependent on the onset of necking which triggers material failure. Although necking and fracture are essentially different events, the first one is an early indication of ultimate structural failure and therefore it is commonly used as a reference for evaluating the energy absorption capacity (Rodríguez-Martínez et al., 2013a), combined with the fact that determination of the stress and strain states after necking presents some difficulties.

According to Considère (1885), necking inception takes place, under quasi-static conditions, when the stress equals the strain hardening, coinciding with the maximum load in the specimen – actually localization starts slightly after the maximum load as pointed out later by Hill (1958). Thus, materials with a high strain hardening are preferred for energy-absorption applications. Moreover, it is commonly accepted that metallic materials for crash, impact or blast protection have

to show a high strain hardening, whatever the range of strain rates. Among the metallic materials having these specific features, steel grades showing *Strain Induced Martensitic Transformation* (SIMT) are widely used for energy absorption in crash or blast protection applications (Andersson, 2005; Langdon and Schleyer, 2005, 2006; Bleck et al., 2005; Sato et al., 2013). Their ability to transform from the initial face-centered cubic austenite phase γ to body-centered cubic martensite α' during plastic deformation is comparable to a dynamic composite effect and causes a remarkable hardening (Lichtenfeld et al., 2006; Oliver et al., 2007; Dan et al., 2008). Multiphase TRansformation Induced Plasticity (TRIP) steels and metastable austenitic grades are representative examples of steels exhibiting SIMT. It is worth pointing out that SIMT is markedly affected by temperature, which stabilizes the austenitic phase (Olson and Cohen, 1975). Therefore, the beneficial effect of phase transformation may be cancelled at high temperatures.

Under dynamic conditions, as in quasi-static conditions, strain hardening keeps contributing to delay necking formation (Ghosh, 1977; Xue et al., 2008) and a new effect starts to play a stabilizing role: *inertia*. In this context, the term inertia accounts for the intrinsic material effects that density, sample dimensions, flow stress and loading rate all have on necking inception, as stated by different authors (Knoche and Needleman, 1993; Mercier and Molinari, 2003, 2004; Zhou et al., 2006; Vadillo et al., 2012). For instance, Zhou et al. (2006) derived a dimensionless number $\bar{I}$ to account for all these factors within a 1D framework

$$\bar{I} = \frac{\sqrt{\sigma_0/\rho}}{r_0\dot{\varepsilon}} \tag{1}$$

σ_0 being the yield stress, ρ the density, r_0 a characteristic dimension and $\dot{\varepsilon}$ the strain rate. In a dimensionless form of the equation of movement for the problem formulation of dynamically stretching 1D solids, $1/\bar{I}^2$ is the factor multiplying the acceleration, thus representing the inertial resistance to motion. As $\bar{I}$ decreases the material behavior is stabilized, delaying the formation and development of plastic instabilities. Actually, at high deformation rates, inertia may take the dominant role in stabilizing the material, on top of the hardening effects. As reported in the theoretical work by Rodríguez-Martínez et al. (2013a), at high loading rates, a strong strain hardening may not provide the expected material ductility increase. The cause of this behavior, specifically observed in steels showing SIMT, requires further analysis.

Therefore, we present a theoretical approach to evaluate the interplay between strain induced martensitic transformation and inertia on the ductility and energy absorption capacity of materials subjected to dynamic loading. The study is performed considering the dynamic stretching of a cylindrical slender bar, and two complementary methodologies are used: linear stability analysis and finite element simulations. The results obtained with the second method (necking strain, necking wavelength, energy dissipated by plastic flow) at different strain rates and for different kinetics of transformation are rationalized with the first one, permitting to determine the conditions for the development of plastic instabilities. The work considers a metastable austenitic stainless steel as reference material, since this type of grade shows a large amount of transformed martensite even under adiabatic conditions (Rodríguez-Martínez et al., 2011). The study allows to analyze the range of strain rates at which the beneficial effect of transformation hardening on material ductility and energy absorption capacity becomes masked by the inertial effects. In this case, alloys with lower transformation hardening may show larger ductilities or higher energy absorption rates. The analysis permits to draw relevant conclusions about the use of steels exhibiting SIMT in high loading rate applications.

2. Constitutive model for SIMT in metastable austenitic steels

The constitutive model for the metastable austenitic stainless steel uses Huber–Mises plasticity and the features related to martensitic transformation are based on the previous works of Olson and Cohen (1975), Stringfellow et al. (1992) and Zaera et al. (2012, 2013). Since inception and development of necks in a slender bar will be analyzed using linear stability – derived within a 1D framework – and finite element simulations – developed within a 3D framework –, both one-dimensional and three-dimensional approaches will be presented, on the understanding that both coincide in their essential features and that, for a uniaxial state of stress, the 3D model provides the same results as its 1D counterpart.

2.1. 1D model: martensitic transformation and yield condition

In the present paper, we consider the closed-form expression proposed by Olson and Cohen (1975), which relates the volumetric fraction of martensite f_m with the plastic strain in the austenite $\bar{\varepsilon}_a^p$ on the hypothesis of intersection of shear bands in austenite as the dominant mechanism of SIMT

$$f_m = 1 - \exp\left[-\beta(1-\exp(-\alpha\bar{\varepsilon}_a^p))^n\right] \tag{2}$$

n being the exponent relating shear bands with shear band intersections through a power law, α a temperature dependent parameter representing the rate of shear-band formation, and β a temperature dependent parameter proportional to the probability that a shear band intersection will form an embryo. As stated by Olson and Cohen (1975), the saturation level in the martensitic transformation is determined by the β parameter, while the rate of approach to saturation is controlled by both α and β.

Austenite plays the role of the soft phase in the material deformation behavior: the strain as well as the strain rate of the austenite are quite close to the homogenized ones and much larger than those corresponding to the martensite (Zaera et al., 2012).

Therefore, the plastic deformation in the austenite $\overline{\varepsilon}_a^p$ and the plastic deformation of the steel $\overline{\varepsilon}^p$ are considered equivalent in the current approach, and Eq. (2) leads to

$$f_m = 1 - \exp\left[-\beta(1-\exp(-\alpha\overline{\varepsilon}^p))^n\right] \tag{3}$$

The closed-form solution provided by Eq. (3) to capture the dependence of the transformed martensite in terms of strain and temperature, instead of using an evolution law, presents the advantage of its simplicity, specifically for analytical approaches like the linear stability analysis that will be developed later. According to Zaera et al. (2012), the following phenomenological law is proposed to fit the dependence of α on temperature

$$\alpha = \alpha_0[1 - \Theta \exp(\alpha_1(1-\Theta^{-1}))] \tag{4}$$

where α_0, α_1 are the material constants, and Θ is the normalized temperature related to the absolute one T by

$$\Theta = \frac{T - M_s^\sigma}{M_d - M_s^\sigma} \tag{5}$$

M_d being the upper temperature limit for phase transformation and M_s^σ the lower limit temperature for strain-induced martensitic nucleation.

The parameter β is proportional to the probability P that a shear band intersection will form an embryo

$$\beta = \beta_0 P \tag{6}$$

β_0 being a dimensionless material constant. Following Stringfellow et al. (1992), a Gaussian cumulative probability distribution function to calculate P is used

$$P(g) = \frac{1}{\sqrt{2\pi}s_g}\int_{-\infty}^{g}\exp\left[-\frac{1}{2}\left(\frac{\tilde{g}-\overline{g}}{s_g}\right)^2\right]d\tilde{g} \tag{7}$$

$\overline{g}$ and s_g being respectively the mean and standard deviation of the normal distribution function. g is a normalized thermodynamic driving force for the martensitic transformation, dependent on temperature. Following Zaera et al. (2012), this dependence is captured with an exponential function

$$g = g_0 \exp(g_1\Theta) \tag{8}$$

where g_0 and g_1 are dimensionless constants. This way, P is temperature dependent through their relation to the driving force g. Triaxiality is known to influence SIMT and its effect can be quantified through an additional term in the driving force, as proposed by Stringfellow et al. (1992). However, the authors concluded in a previous work (Zaera et al., 2012) that hardening in AISI 304 steel is weakly affected by this issue, unless stress states with large differences in the triaxiality are compared. Since variations of the triaxiality along the neck are found in the present study to be small (around 10% when the necking is localized), its effect has been neglected in both the 1D and 3D approaches.

Likewise, the Lode angle φ, defined as

$$\varphi = 1 - \frac{2}{\pi}\arccos\left(\frac{3\sqrt{3}}{2}\frac{J_3}{\sqrt{J_2^3}}\right) \tag{9}$$

J_2 and J_3 being respectively the second and third invariants of the deviatoric stress tensor, is known to modify the kinetics of SIMT (Beese and Mohr, 2011, 2012). The value of the Lode angle under uniaxial stress is equal to one upon homogeneous deformation. Moreover its value keeps very close to one at localized necking (variations across the section with respect to unity below 5%), as it has been verified by the authors. Since the parameters considered for the kinetics of phase transformation were obtained from several works in which the transformation process took place under uniaxial stress conditions, the model accounts implicitly for the effect of the Lode angle. Other problems involving loading paths different than the one considered in this work, such as the analysis of necking inception in biaxially loaded sheets, would certainly require a different approach to capture the influence of the stress state (including stress triaxiality and Lode angle) not only in the kinetics of SIMT (Beese and Mohr, 2011, 2012) but also in the overall stability of the perturbation in biaxial conditions (Dudzinski and Molinari, 1991).

The effective yield stress in the two-phase steel σ_Y is calculated by the rule of mixtures

$$\sigma_Y = \Psi(f_m) = (1-f_m)\sigma_Y^a + f_m\sigma_Y^m \tag{10}$$

where σ_Y^a and σ_Y^m are the yield stress of the austenite and of the martensite respectively. There are other methods allowing to obtain homogeneous properties for multiphase materials in a more rigourous way, such as the procedure described in Papatriantafillou et al. (2006) and Zaera et al. (2012), but the one proposed above is especially suitable within the frame of the linear stability approach that will be described and used later. Additionally, the yield stress of both austenite and martensite have been considered constant, neglecting any functional dependence on strain, strain rate and temperature. The influence that strain hardening, strain rate sensitivity and temperature sensitivity have on dynamic plastic instabilities has been discussed in a number of relevant works (Fressengeas and Molinari, 1985, 1994; Han and Tvergaard, 1995; Hu and Daehn, 1996; Sørensen and Freund, 1998; Shenoy and Freund, 1999; Mercier and Molinari, 2003, 2004). In these publications the stabilizing effect that strain hardening and strain rate sensitivity have on necking inception and the destabilizing effect of thermal softening was proven. It is worth noting that neglecting

the functional dependence of the material behavior with strain hardening, strain rate sensitivity and temperature sensitivity greatly simplifies the yield stress description. However it has to be highlighted that this procedure allows for a proper evaluation of the role that transformation hardening has in necking inception. This point is particularly relevant since the authors are unaware of any similar study in which a stability analysis is specifically developed to investigate the effect of martensitic transformation on dynamic flow localization.

The yield condition may be written as

$$\Phi = \overline{\sigma} - \Psi(f_m) = 0 \tag{11}$$

$\overline{\sigma}$ being the equivalent stress. The previous expression highlights the effect of martensitic transformation as unique source of hardening that, according to the perfect-plasticity hypothesis adopted for the phases, can be denoted as *transformation hardening*.

According to Eqs. (4) and (8), there is a coupling between phase transformation and temperature; therefore the energy balance plays a role in the mechanical behavior of the material. Assuming adiabatic conditions, a hypothesis commonly adopted for dynamic applications, the energy balance can be stated as

$$c\frac{\partial T}{\partial t} = \chi\overline{\sigma}\frac{\partial \overline{\varepsilon}^p}{\partial t} + \frac{\partial f_m}{\partial t} l_h \tag{12}$$

where c and χ stand for heat capacity per unit volume and Taylor–Quinney coefficient respectively. l_h is the latent heat per unit volume of transformed austenite, therefore the last term in the above equation accounts for the heat released due to the exothermic character of the phase transformation. This has been reported by different authors for dynamically phase transforming materials (Rittel et al., 2006; Jovic et al., 2006; Rusinek and Klepaczko, 2009) and rationalized in Zaera et al. (2013). By virtue of its contribution, the heat power may strongly increase upon a certain range of strain, thus enhancing the coupling between temperature and transformation: SIMT contributes to heat through a latent heat term and heat, in turn, hinders SIMT. Both transformation hardening and its link with thermal effects will be considered in the study of plastic flow localization.

2.2. 3D model

The previous 1D constitutive model may be extended to a 3D framework. Here, the above equations are complemented with the generalized Hooke law for hypoelastic–plastic materials

$$\boldsymbol{\sigma}^{\nabla} = \mathbf{C} : \mathbf{d}^e = \mathbf{C} : (\mathbf{d} - \mathbf{d}^p) \tag{13}$$

where $\boldsymbol{\sigma}^{\nabla}$ is an objective derivative of the Cauchy stress tensor, $\mathbf{d}$, $\mathbf{d}^e$ and $\mathbf{d}^p$ are respectively the total, elastic, and plastic rate of deformation tensors, and $\mathbf{C}$ is the Hooke tensor for isotropic elasticity, defined by the elastic bulk modulus K and elastic shear modulus G. Additionally, an associated flow rule is considered

$$\mathbf{d}^p = \dot{\lambda}\frac{\partial \Phi}{\partial \boldsymbol{\sigma}} = \dot{\lambda}\frac{3}{2}\frac{\mathbf{s}}{\overline{\sigma}} \tag{14}$$

λ being the plastic multiplier, which coincides with the equivalent plastic strain in Huber–Mises plasticity, and $\mathbf{s}$ the deviatoric stress tensor.

Table 1 shows the values of the model parameters for the AISI 304 grade, as taken from Zaera et al. (2012, 2013). σ_Y^a and σ_Y^m were adopted as representative of the plastic flow stress in austenite and martensite, respectively (Zaera et al., 2012).

3. Problem formulation and linear stability analysis

The linear stability analysis presented next is based on previous works (Fressengeas and Molinari, 1985; Zhou et al., 2006) and includes specific features to account for martensitic transformation and its associated thermodynamic effects.

3.1. Governing equations

Let us consider a cylindrical bar of initial length L_0, circular cross section radius r_0 and area $A_0 = \pi r_0^2$. The bar is subjected to a constant stretching velocity on both sides. It is supposed that this loading condition is always satisfied, and therefore elastic unloading is disregarded. The bar material is taken to be incompressible, of mass density ρ, with a mechanical behavior described by a simplified constitutive relation (Eq. (10)) linking the yield stress σ_Y with the volumetric fraction of martensite f_m (given by Eq. (3)), which in turn depends on strain and temperature

$$\sigma_Y = \Psi(f_m) \tag{15}$$

The true strain ε and the strain rate $\dot{\varepsilon}$ are defined as $\varepsilon = \ln[(\partial x/\partial X)_t]$ and $\dot{\varepsilon} = \partial\varepsilon/\partial t$, X being the Lagrangian coordinate ($-L_0/2 \le X \le L_0/2$), and x the Eulerian coordinate given by

$$x = X + \int_0^t v(X,\tau)\, d\tau \tag{16}$$

Table 1
Parameters related to transformation kinetics and yield stresses, elastic moduli, and conventional physical constants for AISI 304 steel (Zaera et al., 2012, 2013).

Symbol	Property and units	Value
n	Dimensionless material constant, Eq. (3)	4.5
α_0	Dimensionless material constant, Eq. (4)	8.5
α_1	Dimensionless material constant, Eq. (4)	0.59
g_0	Dimensionless material constant, Eq. (8)	-30.0
g_1	Dimensionless material constant, Eq. (8)	4.10
$\overline{g}$	Dimensionless mean of P distribution, Eq. (7)	-87
s_g	Dimensionless standard deviation of P distribution, Eq. (7)	129.5
β_0	Dimensionless material constant, Eq. (6)	14.5
M_d	Upper limit temperature for SIMT (K), Eq. (10)	443
M_s^σ	Lower limit temperature for SIMT (K), Eq. (10)	173
l_h	Specific transformation latent heat (MJ/m^3), Eq. (12)	118
σ_Y^a	Yield stress of the austenite (MPa), Eq. (5)	300
σ_Y^m	Yield stress of the martensite (MPa), Eq. (5)	900
G	Elastic shear modulus (GPa)	75.0
K	Elastic bulk modulus (GPa)	199.6
ρ	Density (kg/m^3), Eq. (20)	7800
c	Heat capacity per unit volume (MJ/K m^3), Eq. (12)	3.9
χ	Taylor–Quinney coefficient, Eq. (12)	0.8

where v is the current axial velocity. Since large deformations are considered, elasticity can be neglected. Additionally, considering uniaxial tensile conditions, the following equivalence may be stated: $\overline{\varepsilon}^p = \varepsilon$.

The fundamental equations governing the loading process are presented below:

- Mass conservation:

$$\frac{\partial v}{\partial X} = e^{\varepsilon}\dot{\varepsilon} \tag{17}$$

- Flow stress:

$$\sigma = (1+\theta^{-1})\ln(1+\theta)\sigma_Y \tag{18}$$

where σ is the true stress, defined as the averaged axial stress in the cross-section. The correction factor θ (Bridgman, 1952; Walsh, 1984; Fressengeas and Molinari, 1985) is used to take into account that, in case of necking, the local axial stress is enhanced by the hydrostatic stress. The use of this specialized form of the yield stress is a key point of the model since it allows for damping short wavelength modes, which is consistent with the results published by Rodríguez-Martínez et al. (2013c). The factor θ is defined as

$$\theta = \frac{1}{2}r\left(\frac{\partial^2 r}{\partial x^2}\right) = \frac{2A\left(\frac{\partial^2 A}{\partial x^2}\right) - \left(\frac{\partial A}{\partial x}\right)^2}{8\pi A} = \frac{A_0 e^{-3\varepsilon}}{8\pi}\left(\frac{\partial \varepsilon}{\partial X}\right)^2 - \frac{\partial^2 \varepsilon}{\partial X^2}\Bigg) \tag{19}$$

where the relation $A = A_0 e^{-\varepsilon}$, derived from the incompressibility condition, has been used.

- Momentum balance in the axial direction:

$$\rho\frac{\partial v}{\partial t} = \frac{\partial}{\partial X}(\sigma e^{-\varepsilon}) \tag{20}$$

- Transformation law: from Eq. (3)

$$f_m = F(\varepsilon, \alpha(T), \beta(T)) \tag{21}$$

- Conservation of energy: according to the consideration of the previous section, the loading process is assumed to be adiabatic. Given that $\overline{\sigma} = \sigma$ in uniaxial stress conditions, Eq. (12) yields

$$c\frac{\partial T}{\partial t} = \chi\sigma\dot{\varepsilon} + \frac{\partial f_m}{\partial t}l_h \tag{22}$$

Considering the domain $[-L_0/2, L_0/2]$, Eqs. (17) and (18) and (20)–(22) are to be solved under the following initial conditions formulated in Lagrangian coordinates: $v(X,0) = \dot{\varepsilon}_0 X$; $\sigma(X,0) = \Psi(0) = \sigma_Y^a$; $\varepsilon(X,0) = 0$; $T(X,0) = T_0$; $f_m(X,0) = 0$, and

boundary conditions: $v(L_0/2,t) = -v(-L_0/2,t) = \dot{\varepsilon}_0 L_0/2$; $\partial T(X,t)/\partial X|_{X=L_0/2} = \partial T(X,t)/\partial X|_{X=-L_0/2} = 0$. The constant $\dot{\varepsilon}_0$ defines the value of the initial strain rate in the bar.

One should note that the model does not consider the momentum balance in the radial direction. In this respect Rubin and Rodríguez-Martínez (submitted for publication) showed that, in comparison with longitudinal inertia, radial inertia plays a secondary role stabilizing plastic flow at high strain rates. Therefore the results and conclusions of the present research should not be significantly affected by such simplification, which in turn greatly facilitates the derivation of the stability analysis.

3.2. Linear perturbation analysis

Let $\mathbb{S}(X,t) = (v(X), \sigma(t), \varepsilon(t), T(t), f_m(t))^T$ be the homogeneous time-dependent solution, at time t, of the previous problem. $\mathbb{S}$ is obtained by integration of Eqs. (17) and (18) and (20)–(22) satisfying the initial and boundary conditions previously listed. Since the transformation kinetics is given by the closed-form solution proposed by Olson and Cohen (1975), a monotonic increase condition is required for f_m in order to avoid a decrease of the martensite fraction.

At time $t = t_1$, at which the homogeneous solution reaches the value $\mathbb{S}^1(X,t_1) = (v_1(X), \sigma_1, \varepsilon_1, T_1, f_{m1})^T$, consider a small perturbation of this solution $\delta\mathbb{S}(t_1,X,t)$, with $|\delta\mathbb{S}(t_1,X,t)| \ll |\mathbb{S}^1(X,t_1)|$, given by

$$\delta\mathbb{S}(t_1,X,t) = \delta\mathbb{S}^1 e^{i\xi X} e^{\eta(t-t_1)} \tag{23}$$

where $\delta\mathbb{S}^1 = (\delta v, \delta\sigma, \delta\varepsilon, \delta T, \delta f_m)^T$ is the perturbation amplitude, ξ the wavenumber and η the growth rate of the perturbation at time t_1. The perturbation becomes unstable when $Re(\eta) > 0$. According to Rodríguez-Martínez et al. (2013a) the perturbation growth η^+ is assumed to represent the onset of *diffuse necking*. The term diffuse necking describes the stage of the loading process at which the local plastic flow deviates from the background value.

By substituting Eq. (23) into Eqs. (17) and (18) and (20)–(22) and retaining only first-order terms, the following linearized equations are obtained:

- Mass conservation:

$$\delta v + i\xi^{-1} e^{\varepsilon_1} (\dot{\varepsilon}_1 + \eta)\delta\varepsilon = 0 \tag{24}$$

- Flow stress:

$$\delta\sigma - \sigma_1 \frac{A_0\xi^2}{8\pi} e^{-3\varepsilon_1}\delta\varepsilon - R\delta f_m = 0 \tag{25}$$

- Momentum balance in the axial direction:

$$\rho\eta\delta v - i\xi e^{-\varepsilon_1}\delta\sigma + i\xi\sigma_1 e^{-\varepsilon_1}\delta\varepsilon = 0 \tag{26}$$

- Transformation law:

$$F_\varepsilon\delta\varepsilon + (F_\alpha\alpha_T + F_\beta\beta_T)\delta T - \delta f_m = 0 \tag{27}$$

- Conservation of energy in adiabatic conditions:

$$\chi\dot{\varepsilon}_1\delta\sigma + \chi\sigma_1\eta\delta\varepsilon - c\eta\delta T + l_h\eta\delta f_m = 0 \tag{28}$$

with

$$F_\varepsilon = \left.\frac{\partial F}{\partial\varepsilon}\right|_{t_1}; \quad F_\alpha = \left.\frac{\partial F}{\partial\alpha}\right|_{t_1}; \quad F_\beta = \left.\frac{\partial F}{\partial\beta}\right|_{t_1}$$

$$R = \left.\frac{\partial\Psi}{\partial f_m}\right|_{t_1}; \quad \alpha_T = \left.\frac{d\alpha}{dT}\right|_{t_1}; \quad \beta_T = \left.\frac{d\beta}{dT}\right|_{t_1}$$

A non-trivial solution for $\delta\mathbb{S}^1$ is obtained only if the determinant of the system of linear algebraic equations (24)–(28) is equal to zero. Using the following dimensionless variables and constants:

$$\bar{\eta} = \frac{\eta}{\dot{\varepsilon}_1}; \quad \bar{\xi} = r_0\xi; \quad \psi(f_m) = \frac{\Psi(f_m)}{\sigma_0}$$

$$\bar{I}^2 = \frac{\sigma_0}{\rho r_0^2\dot{\varepsilon}_1^2}; \quad \Lambda = e^{-\varepsilon_1}; \quad \bar{T} = \frac{T_1}{T_{ref}}; \quad \psi_1 = \frac{\sigma_1(t_1)}{\sigma_0}; \quad \bar{l}_h = \frac{l_h}{\sigma_0}$$

$$\tilde{c} = \frac{cT_{ref}}{\sigma_0} - \bar{l}_h\left(F_\beta \beta_{\overline{T}} + F_\alpha \alpha_{\overline{T}}\right); \quad \tilde{P} = \tilde{R}\left(F_\beta \beta_{\overline{T}} + F_\alpha \alpha_{\overline{T}}\right); \quad \tilde{H} = \tilde{R}F_\varepsilon$$

$$\tilde{R} = \left.\frac{\partial \psi}{\partial f_m}\right|_{t_1}; \quad \beta_{\overline{T}} = \left.\frac{d\beta}{d\overline{T}}\right|_{t_1}; \quad \alpha_{\overline{T}} = \left.\frac{d\alpha}{d\overline{T}}\right|_{t_1}$$

with $\sigma_0 = \sigma_Y^a$ and $T_{ref} = T_0$, the resulting condition is found to be a cubic equation in $\overline{\eta}$

$$B_3\overline{\eta}^3 + B_2\overline{\eta}^2 + B_1\overline{\eta} + B_0 = 0 \tag{29}$$

with

$$B_3 = \tilde{c} \tag{30}$$

$$B_2 = \tilde{c} - \tilde{P}\chi \tag{31}$$

$$B_1 = -\tilde{P}\chi + \overline{\xi}^2\overline{I}^2\Lambda^2\left[\tilde{c}\ \ \frac{\overline{\xi}^2}{8}\Lambda^3\psi_1 + \tilde{H} - \psi_1\right) + F_\varepsilon\bar{l}_h\tilde{P} + \tilde{P}\chi\psi_1\Bigg) \tag{32}$$

$$B_0 = \overline{I}^2\tilde{P}\Lambda^2\overline{\xi}^2\chi\psi_1 \tag{33}$$

Summarizing, Eq. (29) gives, for a certain value of the time at perturbation t_1, the values of $\overline{\eta}$ as a function of the dimensionless wavenumber $\overline{\xi}$. The requisite for unstable growth of $\mathbb{S}^1$ is given by the condition $Re(\overline{\eta}) > 0$. Eq. (29) has three roots in $\overline{\eta}$, one real and two complex conjugates. Only the one having the greater positive real part has to be considered for the analysis of the dimensionless perturbation growth rate $\overline{\eta}^+$. Moreover, imposing the condition for maximum perturbation growth $\partial\overline{\eta}^+/\partial\overline{\xi} = 0$, the critical wavenumber $\overline{\xi}_c$ and the critical perturbation growth $\overline{\eta}_c^+$ are determined.

It is important to note here that the stability analysis does not allow for calculation of the necking strain, but permits identifying the dependences of necking strain and necking pattern with material behavior. The necking strain correlates with the critical perturbation growth and the necking pattern correlates with the dominant wavenumber (see Zhou et al., 2006 and Vadillo et al., 2012 for further details).

3.2.1. Particular case: isothermal loading process

Isothermal loading processes will be considered in some of the following studies, and this case is obtained disregarding Eq. (28) in the analysis. Under this assumption, a non-trivial solution is possible if the following quadratic expression in $\overline{\eta}$ is accomplished:

$$C_2\overline{\eta}^2 + C_1\overline{\eta} + C_0 = 0 \tag{34}$$

with

$$C_2 = C_1 = 1; \quad C_0 = \overline{I}^2\Lambda^2\overline{\xi}^2\ \ \tilde{H} + \psi_1\ \ \frac{\overline{\xi}^2}{8}\Lambda^3 - 1\Bigg)\Bigg) \tag{35}$$

Then, the condition to have one positive real root is written as

$$\psi_1\ \ \frac{1-\overline{\xi}^2}{8}\Lambda^3\Bigg) > \tilde{H} \tag{36}$$

and the root is given by the expression

$$\overline{\eta}^+ = \frac{1}{2}\left[-1 + \sqrt{1 + 4\overline{I}^2\Lambda^2\overline{\xi}^2\left(\psi_1\left(\frac{1-\overline{\xi}^2}{8}\Lambda^3\right) - \tilde{H}\right)}\right] \tag{37}$$

Likewise, closed-form solutions for $\overline{\xi}_c$ and $\overline{\eta}_c^+$ may be found (Vadillo et al., 2012).

4. Finite element modeling of the dynamic expansion of a ductile cylindrical bar

This section describes the features of the axisymmetric finite element model developed to simulate the rapid stretching of a ductile cylindrical bar. The numerical analyses are carried out using the finite element program ABAQUS/Explicit (Simulia, 2013). The dimensions of the cylindrical bar are $L_0 = 2 \times 10^{-2}$ m of initial length, and $r_0 = 5 \times 10^{-4}$ m of initial radius. Due to the symmetry of the model, only the $z \geq 0$ half of the specimen needs to be analyzed (see Fig. 1). The bar has been meshed using a total of 2000 four-node axisymmetric reduced integration elements (10 elements in the radial direction and 200 elements along the half-length), CAX4R in ABAQUS notation, with an element aspect ratio equal to 1:1 (Fig. 1). To prevent hourglass deformation modes, the viscous method available in ABAQUS/Explicit has been used, with a scale factor for all hourglass stiffnesses equal to one. A mesh convergence study has been performed, and the time evolution of different critical output variables, namely stress, strain and necking inception, were compared against a measure of mesh

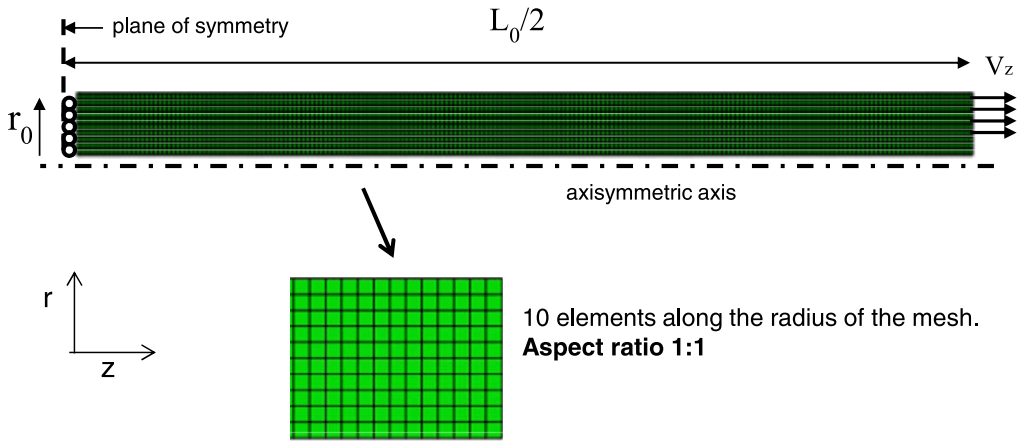

Fig. 1. Finite element mesh and mechanical boundary conditions of the cylindrical bar, modeled as an axially symmetric specimen.

density until the results converged satisfactorily. Neither geometrical nor material imperfections were introduced into the model, being the numerical round-off sufficient to perturb the stress and the strain fields (Rusinek and Zaera, 2007; Vadillo et al., 2012; Rodríguez-Martínez et al., 2013a).

The imposed loading conditions can be formulated as $V_z(r, L/2, t) = \dot{\varepsilon}_0 L_0/2$, $V_z(r, 0, t) = 0$. In order to avoid the propagation of waves along the bar, caused by the application of these boundary conditions in a solid at rest showing elastic behavior, specific initial conditions consistent with the boundary conditions should be imposed. Considering a homogeneous uniaxial stress state a time $t=0$, the velocity gradient tensor in cylindrical coordinates may be written as (hypoelasticity and zero spin tensor)

$$\mathbf{l}_0 = \mathbf{d}_0^e + \mathbf{d}_0^p = \begin{pmatrix} -\nu\dot{\varepsilon}_0^e - \dot{\varepsilon}_0^p/2 & 0 & 0 \\ 0 & -\nu\dot{\varepsilon}_0^e - \dot{\varepsilon}_0^p/2 & 0 \\ 0 & 0 & \dot{\varepsilon}_0^e + \dot{\varepsilon}_0^p \end{pmatrix} \tag{38}$$

Then, the radial and axial initial velocities fields – needed for the axisymmetric FE model – are obtained by integration of the above tensor, leading to

$$V_r(r, z, 0) = -(\nu\dot{\varepsilon}_0^e + \dot{\varepsilon}_0^p/2)r \tag{39}$$

$$V_z(r, z, 0) = (\dot{\varepsilon}_0^e + \dot{\varepsilon}_0^p)z \tag{40}$$

For hypoelastic–plastic materials with $\dot{\varepsilon}_0 = \dot{\varepsilon}_0^e + \dot{\varepsilon}_0^p \simeq \dot{\varepsilon}_0^p$, the initial conditions can be simplified as

$$V_r(r, z, 0) = -\frac{\dot{\varepsilon}_0}{2} r \tag{41}$$

$$V_z(r, z, 0) = \dot{\varepsilon}_0 z \tag{42}$$

Likewise, in order to avoid the abrupt jump in the stress field caused by application of the boundary conditions, the material flow has been initialized in the whole domain with a value of σ_z equal to the initial yield stress of the material. If neither the velocity nor the stress fields were initialized, for sufficiently high velocities the generated wave could induce by itself a neck (Needleman, 1991; Xue et al., 2008). Regarding initial thermal conditions, T_0 has been taken equal to 293 K in all cases. The whole model was defined with a script to allow the rapid definition of initial an boundary conditions in consonance with the particular loading case considered.

The set of constitutive equations describing martensitic transformation are implemented in the finite element code through a user subroutine. For its integration in a finite deformation framework, incremental objectivity is achieved by rewriting them in a corotational configuration (Simó and Hughes, 1998; Doghri, 2000), defined in ABAQUS/Explicit by the polar rotation tensor. The stress is updated with the radial return algorithm

$$\boldsymbol{\sigma}_{n+1} = \boldsymbol{\sigma}_{n+1}^{trial} - 3G\Delta\bar{\varepsilon}^p \frac{\mathbf{s}_{n+1}}{\bar{\sigma}_{n+1}} \tag{43}$$

where the trial stress is defined by

$$\boldsymbol{\sigma}_{n+1}^{trial} = \boldsymbol{\sigma}_n + \mathbf{C} : \Delta\boldsymbol{\varepsilon} \tag{44}$$

According to the properties of radial return, the equivalent stress may be updated with the following equation:

$$\bar{\sigma}_{n+1} = \bar{\sigma}_{n+1}^{trial} - 3G\Delta\bar{\varepsilon}^p \tag{45}$$

and the yield condition (Eq. (11)), coupled to the kinetics of martensitic transformation defined by Eq. (3), permits to obtain the equivalent plastic strain increment $\Delta\bar{\varepsilon}^p$.

Next, results of the finite element computations and stability analysis are presented. The analysis is divided into three parts:

1. *Isothermal loading process*: neither the stability analysis nor the finite element modeling take into account the thermomechanical coupling in the material behavior. The transformation kinetics is assumed temperature independent. Thus, this section pays exclusive attention to the roles that inertia and transformation hardening play in necking inception and energy absorption capacity of the material.
2. *Adiabatic loading process*: both the stability analysis and the finite element modeling take into account the thermomechanical coupling in the phase transformation kinetics according to the experimental observations reported elsewhere (Olson and Cohen, 1975; Tomita and Iwamoto, 1995; Rodríguez-Martínez et al., 2011; Zaera et al., 2012, 2013). Thus, this section examines the effect of temperature on the transformation rate which, in turn, affects the transformation hardening and consequently the processes of necking inception and energy absorption.
3. *The role played by the transformation kinetics on necking inception and energy absorption capacity*: both the stability analysis and the finite element modeling take into account the thermomechanical coupling in the phase transformation kinetics. A systematic analysis on the effect that the transformation rate and volume fraction of martensite at saturation have on necking inception and energy absorption capacity of the material is conducted.

5. Isothermal loading process

According to the material parameters listed in Table 1, Fig. 2 illustrates the dimensionless flow stress upon plastic strain of the soft phase (austenite), the hard phase (martensite) and the material developing transformation (SIMT), in an isothermal loading process. The SIMT material shows an initial yield stress coincident with that prescribed for austenite (in the undeformed state, the material is composed of 100% austenite). As deformation proceeds, the martensitic transformation develops which increases the flow stress and transformation hardening of the material. The maximum transformation rate is displayed at $\bar{\varepsilon}^p \sim 0.2$, at this point the strain hardening curve turns from concave up to concave down. The maximum volume fraction of martensite is reached at $\bar{\varepsilon}^p \sim 0.7$, once the transformation is complete, the SIMT material hardens no more. Then, $\sim 95\%$ of the austenite has been transformed to martensite, i.e. once the transformation is complete the SIMT material shows slightly lower flow stress than martensite. Similar volume fractions of martensite have been experimentally measured in austenitic steels tested in tension under isothermal conditions of deformation, see Rodríguez-Martínez et al. (2011).

Next, we will show results of the stability analysis and the finite element simulations within wide ranges of loading rates. At this point it is convenient to highlight the contribution of inertia effects stabilizing plastic flow. This translates into (a) decreasing perturbation growth rates as the loading rate increases and (b) increasing necking strain as the loading rate increases. This behavior will be discussed in detail in the following sections of the paper.

5.1. Stability analysis results

Next, the results obtained from the stability analysis are discussed. Here, it is important to emphasize the relation between critical perturbation growth and necking strain. The stability analysis provides $\overline{\eta}_c^+$, whereas necking strain will be obtained from finite element simulations.

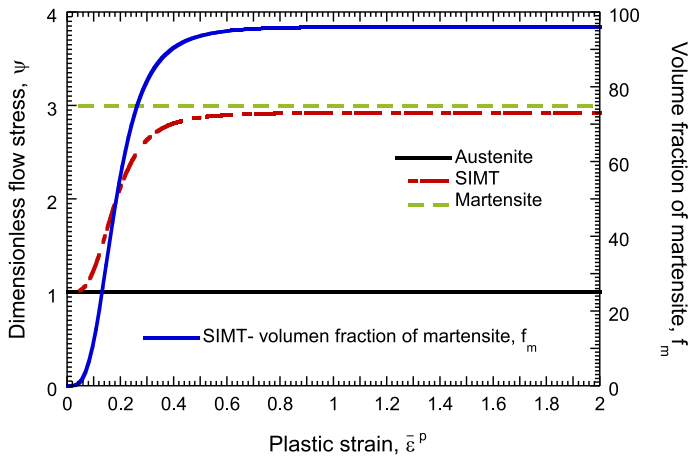

Fig. 2. Dimensionless flow stress versus equivalent plastic strain for austenite, martensite and SIMT material in an isothermal loading process. Corresponding volume fraction of martensite.

Fig. 3 illustrates the dimensionless critical perturbation growth $\overline{\eta}_c^+$ versus plastic strain at perturbation ε_1 for austenite, martensite and the SIMT material. Two different loading rates are analyzed: $\dot{\varepsilon}_0 = 5000\ s^{-1}$ in Fig. 3a and $\dot{\varepsilon}_0 = 20\,000\ s^{-1}$ in Fig. 3b. It must be highlighted that as the loading rate increases the critical perturbation growth decreases. In other words, the strain rate boosts the role played by inertia in the material response, stabilizing the plastic flow and delaying the strain localization process. Therefore one should expect that, as the loading rate increases, the necking strains also do. This behavior finds good agreement with the experimental evidences reported for a number of metals and alloys in Grady and Benson (1983), Regazzoni and Montheillet (1985), Altynova et al. (1996), and provides further validation to the role played by inertia in neck retardation predicted by stability analysis and finite element simulations, as discussed in forthcoming sections of the paper.

Now, we pay attention to the differences between the $\overline{\eta}_c^+ - \varepsilon_1$ curves corresponding to each material considered in this analysis. Note that the discussion conducted below applies for any loading rate. For the sake of clarity, the relation $\overline{\eta}_c^+ - \varepsilon_1$ is analyzed for the phases and the SIMT material in a separate manner:

- Phases: the perturbation grows for any value of plastic strain considered and the critical perturbation growth increases continuously and non-linearly with material straining, i.e. material straining leads to a more unstable material favoring the flow localization. This observation is in agreement with analytical and numerical observations reported elsewhere (Mercier and Molinari, 2003). It should be highlighted that the critical perturbation growth depends on the material flow stress. This is, $\overline{\eta}_c^+$ is lower for the austenite than for the martensite since the latter displays larger yield stress, hence decreasing the inertial resistance to motion (see Eq. (1)). Therefore, one should expect that the austenite will show larger ductility than the martensite. Note also that, as the plastic strain increases, the gap between the phases increases. Therefore, if necking develops for large values of strain, it is expected that the difference between the ductilities of austenite and martensite will increase.
- SIMT: for $\varepsilon_1 = 0$ the critical perturbation growth is identical to that predicted for austenite since formerly the material is composed of 100% austenite. The critical perturbation growth decreases with material straining until $\overline{\eta}_c^+ = 0$ for

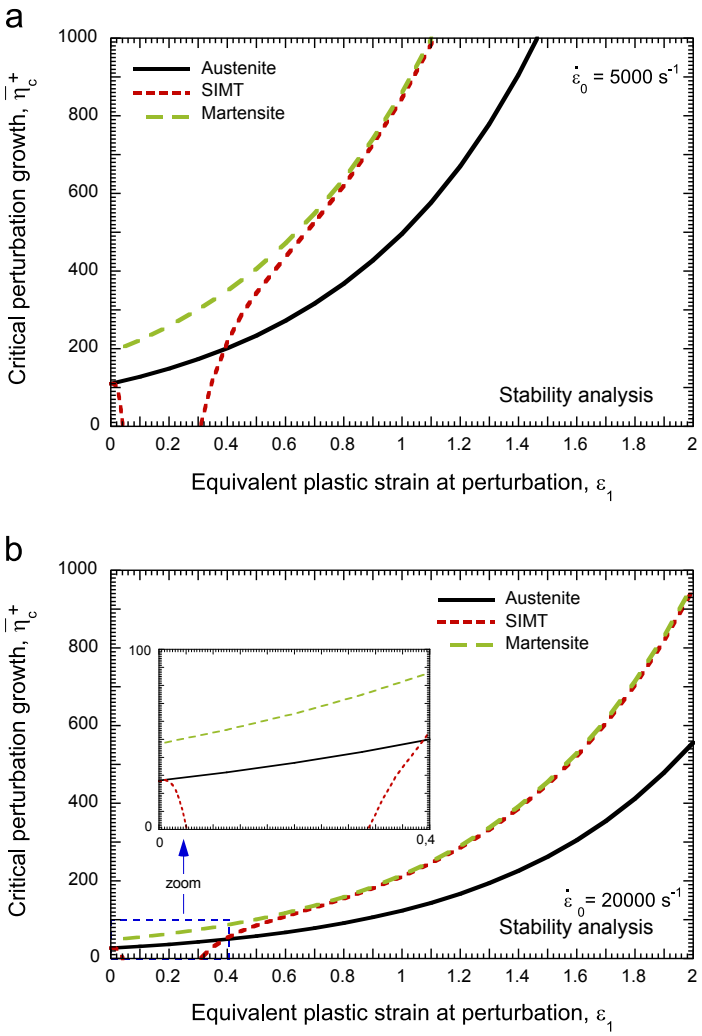

Fig. 3. Critical perturbation growth versus equivalent plastic strain at perturbation for austenite, martensite and SIMT material in an isothermal loading process at (a) $\dot{\varepsilon}_0 = 5000\ s^{-1}$, (b) $\dot{\varepsilon}_0 = 20\,000\ s^{-1}$. Results from linear stability analysis.

$\varepsilon_1 \sim 0.04$. This level of plastic straining is such that condition $\psi_1\left(1-\overline{\xi}^2/8\Lambda^3\right)=\tilde{H}$ (see Eq. (36)) is fulfilled. Then, within a range of plastic strains $0.04 \lesssim \varepsilon_1 \lesssim 0.31$ flow localization is precluded since $\psi_1(1-\overline{\xi}^2/8\Lambda^3)<\tilde{H}$. For $\varepsilon_1 > 0.31$ the transformation hardening is lower than the flow stress $\psi_1(1-\overline{\xi}^2/8\Lambda^3)>\tilde{H}$, the material becomes unstable and the perturbation grows again. Then, the $\overline{\eta}_c^+ - \varepsilon_1$ curve calculated for the SIMT material eventually exceeds that corresponding to the austenite. This is caused by the lower flow stress which characterizes the austenite behavior. Moreover, as deformation proceeds, the critical perturbation growth calculated for the SIMT material becomes largely similar to that corresponding to the martensite. The small gap between both curves is ascribed to the slightly different flow stress shown by the martensitic phase and the SIMT material at large strains. Therefore, if necking develops for large values of strain, it is expected that ductility of the martensite and of the SIMT material will be almost identical, and lower than that of the austenite.

Next, results of the finite element computations are presented and rationalized based on the linear stability analysis.

5.2. Finite element results

The localized necking strain $\overline{\varepsilon}^p_{neck}$ has been determined in the numerical computations following the procedure reported elsewhere (Triantafyllidis and Waldenmyer, 2004; Xue et al., 2008; Rodríguez-Martínez et al., 2013a,b). The localized necking strain (from this point designated indistinctly as necking strain) is assumed as determined by the condition $d\overline{\varepsilon}^p/dt = 0$, where $\overline{\varepsilon}^p$ is measured within the unloading zone which surrounds the neck. The term localized necking describes the stage of the loading process for which plastic flow is fully concentrated in the neck region.

Fig. 4 shows the localized necking strain $\overline{\varepsilon}^p_{neck}$ measured for austenite, martensite and the SIMT material upon a wide range of initial strain rates $1\ s^{-1} \leq \dot{\varepsilon}_0 \leq 10^5\ s^{-1}$. Consistent with the procedure followed in the previous section, the relation $\overline{\varepsilon}^p_{neck} - \dot{\varepsilon}_0$ is analyzed for the phases and the SIMT material separately:

- Phases: the necking strain continuously and non-linearly increases with the loading rate. This agrees with the results obtained from the stability analysis which predicted a decrease of the critical perturbation growth as the strain rate increases.
  For strain rates within the range $1\ s^{-1} < \dot{\varepsilon}_0 < 1000\ s^{-1}$ the contribution of inertia to the loading process seems to be rather limited and the necking strain for austenite and martensite is close to zero. If inertia does not play a dominant role in the loading process the plastic flow becomes unstable at the very early stages of the loading process – due to the definition of the phases as perfectly plastic materials. However, the difference between the necking strain of austenite and the necking strain of martensite is already noticeable (the contribution of inertia cannot be neglected). This agrees with the results obtained from the stability analysis which predicted that the ductility of the austenite should be larger than that of the martensite, irrespective of the loading rate.
  For strain rates above $1000\ s^{-1}$ inertia plays a main role in the loading process and the necking strain of the phases experiences a marked increase. Furthermore, the difference between the ductility of the phases increases with the loading rate, i.e. the difference between the ductility of the phases increases as the necking strain does. Such behavior was properly predicted by the stability analysis results as discussed in the previous section.
- SIMT: for strain rates within the range $1\ s^{-1} < \dot{\varepsilon}_0 < 1000\ s^{-1}$ the necking strain for the SIMT material keeps largely constant $\overline{\varepsilon}^p_{neck} \approx 0.3$. This value was identified in the stability analysis as the threshold strain required by the perturbation to develop the second branch of growth illustrated in Fig. 3. This is, the contribution of inertia effects to the loading process (which cannot be neglected within this range of strain rates) and the effect of transformation hardening are

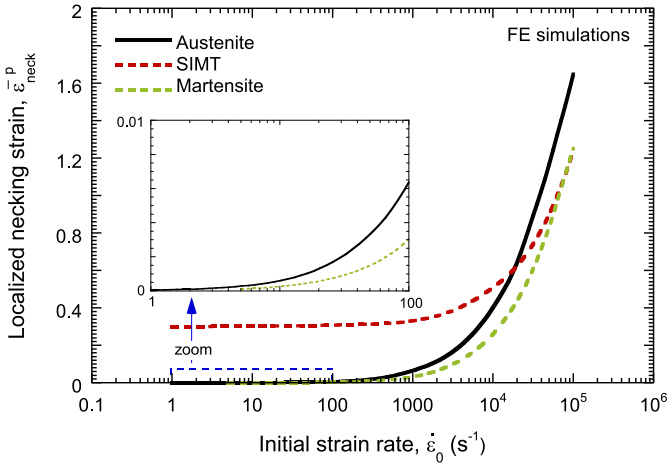

Fig. 4. Localized necking strain versus loading strain rate for austenite, martensite and SIMT material in an isothermal loading process. Results from finite element simulations.

sufficient to overcome the first branch of perturbation growth illustrated in Fig. 3, but necking occurs as soon as the perturbation develops the second branch of growth. At the onset of the second branch of growth – at low loading rates – a small strain increase leads to a drastic rise of the perturbation growth. Thus, the flow stress immediately becomes markedly unstable leading to the rapid inception of necks.

For strain rates above 1000 s^{-1} inertia plays a main role and the necking strain of the SIMT material starts to increase. The necking strain does not correspond to the threshold strain required by the perturbation to develop the second branch of growth illustrated in Fig. 3, since the contribution of inertia is large enough to further delay strain localization. At $\sim 2 \times 10^4$ s^{-1} the curve $\bar{\varepsilon}^p_{neck} - \dot{\varepsilon}_0$ calculated for the SIMT material intersects the curve calculated for the austenite. This is, for strain rates above $\sim 2 \times 10^4$ s^{-1} the austenite develops larger ductility than the SIMT material. This behavior is properly captured by the stability analysis results which predicted that at large strains the critical perturbation growth calculated for the SIMT material exceeds that one calculated for the austenite. Furthermore, for strain rates above $\sim 5 \times 10^4$ s^{-1} the necking strain computed for the SIMT material practically coincides with the one calculated for the martensite. This is in agreement with the observations derived from the stability analysis which predicted largely similar values of $\bar{\eta}_c^+$ for martensite and the SIMT material at large strains.

Previous analysis leads to the following conclusions: (i) there is a clear relation between localized necking strain and strain rate, the first being boosted by the second; (ii) if inertia controls the loading process, the enhanced transformation hardening does not boost the material ductility. Low flow stress materials have better performance in those dynamic applications where large ductility is desired.

Fig. 5 shows the dimensionless specific energy absorbed by austenite, martensite and the SIMT material upon a wide range of initial strain rates $1\ s^{-1} \leq \dot{\varepsilon}_0 \leq 10^5\ s^{-1}$. The dimensionless specific energy $\bar{E}$ is defined by the relation

$$\bar{E} = \frac{\int_0^{\bar{\varepsilon}^p_{neck}} \sigma\, d\varepsilon}{E_{ref}} \tag{46}$$

where E_{ref} is the specific energy absorbed by the austenite per unit strain, i.e. $E_{ref} = 300$ MJ. Following the same procedure of analysis, the relation $\bar{E} - \dot{\varepsilon}_0$ is examined for the phases and the SIMT material separately:

- Phases: as it occurs with the necking strain, the dimensionless specific energy continuously and non-linearly increases with the loading rate. One should note that for any loading rate tested, the dimensionless specific energy absorbed by the martensite is larger than that corresponding to the austenite. This is, although the austenitic phase shows larger ductility, the martensitic phase shows greater capacity for energy absorption thanks to its greater flow stress.
- SIMT: for strain rates within the range $1\ s^{-1} < \dot{\varepsilon}_0 < 2 \times 10^4\ s^{-1}$ the SIMT material displays greater capacity for energy absorption than the phases. It is greater than austenite due to its larger flow stress and ductility and it is greater than martensite due to its larger ductility. However, for strain rates above $2 \times 10^4\ s^{-1}$ the values of $\bar{E}$ calculated for the martensite are greater than those calculated for the SIMT material. Since the yield stress of the martensite is greater than that of SIMT, the energy is also greater at equal ductility.

Thus, the following conclusion arises: at sufficiently high strain rates, when inertia controls the loading process, neither the largest ductility nor the greatest capacity for energy absorption is shown by the SIMT material.

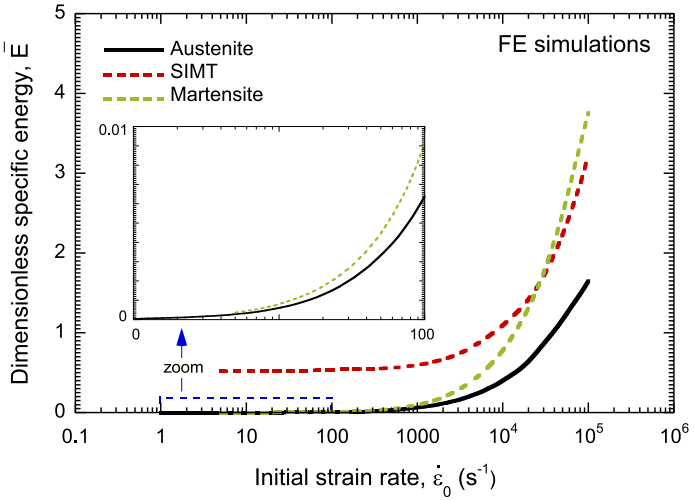

Fig. 5. Dimensionless specific energy versus loading strain rate for austenite, martensite and SIMT material in an isothermal loading process. Results from finite element simulations.

6. Adiabatic loading process

In this section, both the stability analysis and the finite element modeling take into account the thermomechanical coupling in the phase transformation kinetics, as it occurs in a real deformation process.

Fig. 6 illustrates the dimensionless flow stress corresponding to an isothermal loading process (SIMT) – the one analyzed in the previous section – and corresponding to an adiabatic loading process (SIMTT). Both material behaviors show the initial yield stress prescribed for austenite. Subsequently, the onset of deformation triggers the martensitic transformation which enhances the flow stress and transformation hardening. Here the difference between SIMT and SIMTT material behaviors takes place. The effect of adiabatic temperature increase on the transformation kinetics reduces the slope of the stress–strain curve. The temperature dependent kinetics anticipates both the plastic strain corresponding to the maximum transformation rate ($\overline{\varepsilon}^p \sim 0.2$ for SIMT and $\overline{\varepsilon}^p \sim 0.09$ for SIMTT) and the plastic strain at which the maximum volume of martensite is reached ($\overline{\varepsilon}^p \sim 0.7$ for SIMT and $\overline{\varepsilon}^p \sim 0.25$ for SIMTT). In the case of the SIMT material $\sim 95\%$ of the austenite has been transformed to martensite whereas in the case of the SIMTT material the final volume fraction of martensite is $\sim 26\%$. Similar values have been experimentally measured in austenitic steels tested in tension under dynamic (adiabatic) conditions, see Rodríguez-Martínez et al. (2011).

6.1. Stability analysis results

Next, the results obtained from the stability analysis are discussed. Fig. 7 illustrates the dimensionless critical perturbation growth $\overline{\eta}_c^+$ versus strain at perturbation ε_1 for SIMT and SIMTT material behaviors. Two different loading rates are considered: $\dot{\varepsilon}_0 = 3000\ \mathrm{s}^{-1}$ in Fig. 7a and $\dot{\varepsilon}_0 = 40\,000\ \mathrm{s}^{-1}$ in Fig. 7b. It is important to remember here that, unfailingly, the loading rate decreases the critical perturbation growth, thus stabilizing the plastic flow. We pay attention now to the differences between the $\overline{\eta}_c^+$ and ε_1 curves calculated for SIMT and SIMTT materials. The first branch of the $\overline{\eta}_c^+ - \varepsilon_1$ curves is shown largely independent of the constitutive equation. On contrary, the effect of adiabatic temperature increases in the transformation kinetics considerably decreases the upper bound of the range of plastic strains for which the material is stable, from $\varepsilon_1 \approx 0.31$ to $\varepsilon_1 \approx 0.21$. At the onset of the second branch of the curve $\overline{\eta}_c^+ - \varepsilon_1$ the perturbation grow rate is quite similar for both SIMT and SIMTT materials. However, at a certain level of strain at perturbation, the curve calculated for the SIMTT material shows a marked change in slope. This corresponds to the end of the martensitic transformation; from this point on the material behavior becomes temperature independent. As deformation proceeds, the curve calculated for the SIMTT material intersects the one calculated for the SIMT material. For larger values of strain at perturbation the SIMTT material is more stable than the SIMT material because of its lower flow stress. Therefore, if necking develops for low values of strain, it is expected that the ductility of the SIMT material will be larger than that of the SIMTT. Likewise, the trend will be the opposite if necking develops for large values of strain. Bearing in mind that as the loading rate increases the necking strain also does, previous sentence can be rewritten as follows: at low loading rates the ductility of the SIMT material will be larger than that of the SIMTT and for high loading rates the opposite is expected.

Next, results of the finite element computations are presented and rationalized based on the linear stability analysis.

6.2. Finite element results

Fig. 8 shows the localized necking strain measured for SIMT and SIMTT constitutive behaviors upon a wide range of initial strain rates $1\ \mathrm{s}^{-1} \leq \dot{\varepsilon}_0 \leq 5 \times 10^5\ \mathrm{s}^{-1}$. For loading rates below $1000\ \mathrm{s}^{-1}$ the necking strains for both, SIMT and SIMTT behaviors coincide with the threshold strain required by the perturbation to develop the second branch of growth illustrated in Fig. 7. The necking strain is controlled by the transformation hardening, inertia effects play a secondary role in

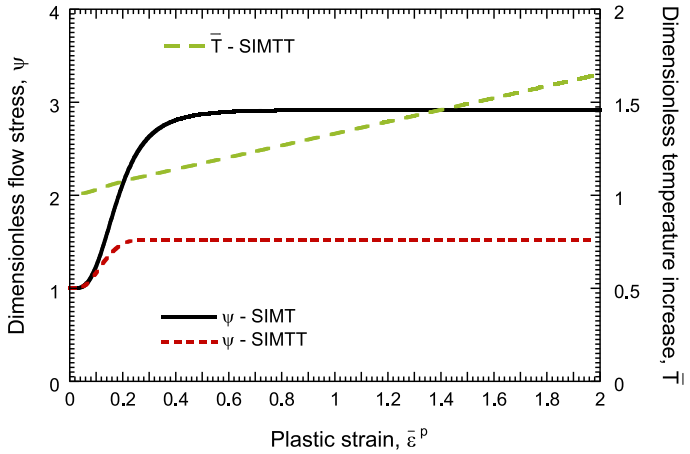

Fig. 6. Dimensionless flow stress versus equivalent plastic strain for SIMT and SIMTT materials. Corresponding temperature evolution with plastic strain.

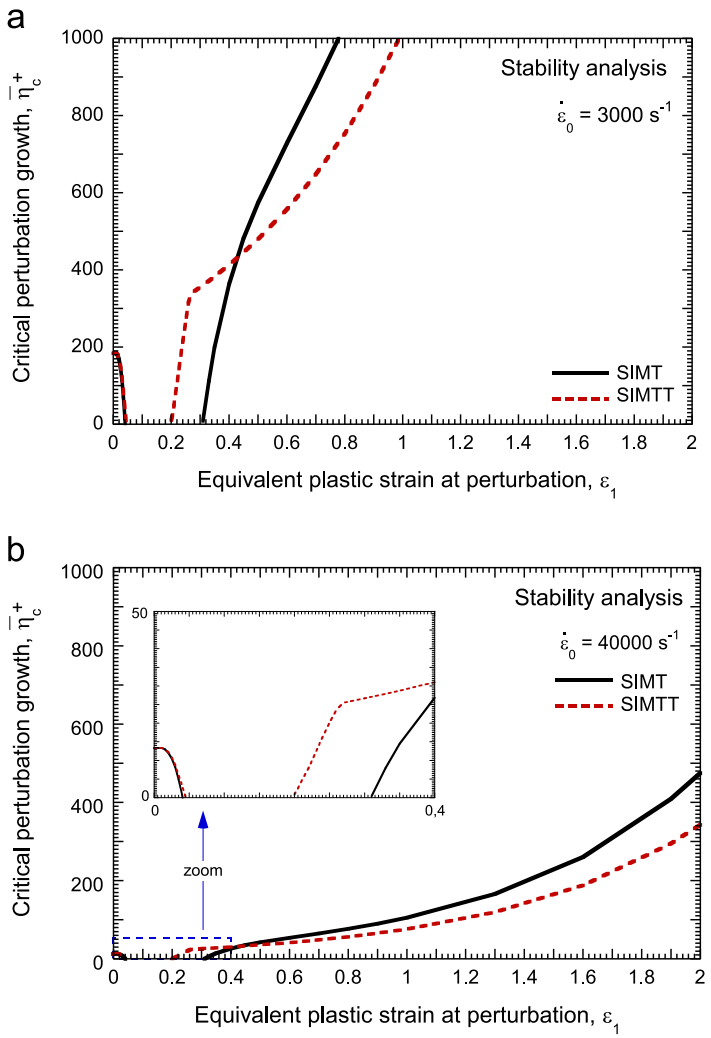

Fig. 7. Critical perturbation growth versus equivalent plastic strain at perturbation for SIMT and SIMTT materials at (a) $\dot{\varepsilon}_0 = 3000\ s^{-1}$, (b) $\dot{\varepsilon}_0 = 40\,000\ s^{-1}$. Results from linear stability analysis.

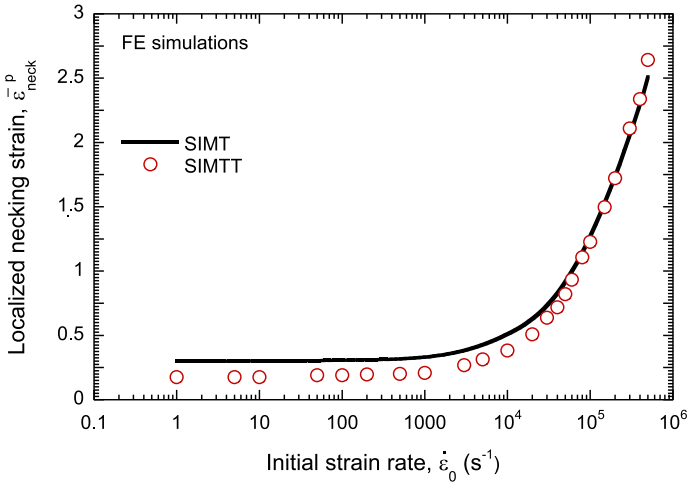

Fig. 8. Localized necking strain versus loading strain rate for SIMT and SIMTT materials. Results from finite element simulations.

the process of flow localization. For loading rates above 1000 s^{-1} the necking strain for both material behaviors increases due to the incipient contribution of inertia. Note here that the rate of growth of the curve calculated for the SIMTT material is greater than that computed for the SIMT material. Thus, approximately for 2×10^5 s^{-1} the necking strain corresponding to the SIMTT material behavior intersects and exceeds that one corresponding to the SIMT.

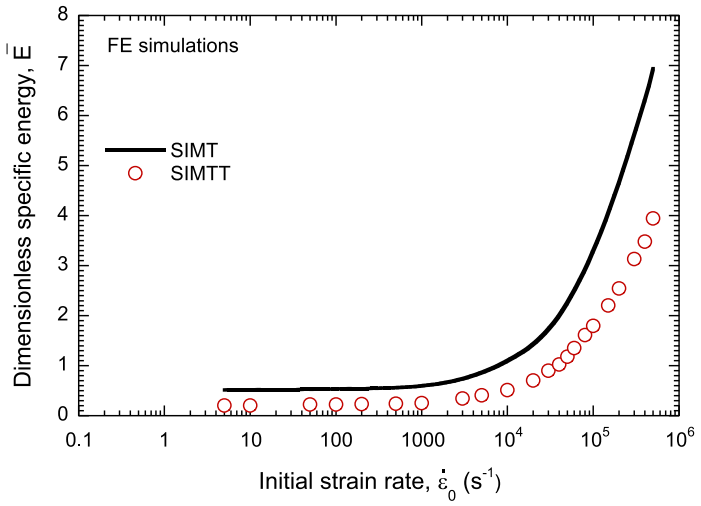

Fig. 9. Dimensionless specific energy versus loading strain rate for SIMT and SIMTT materials. Results from finite element simulations.

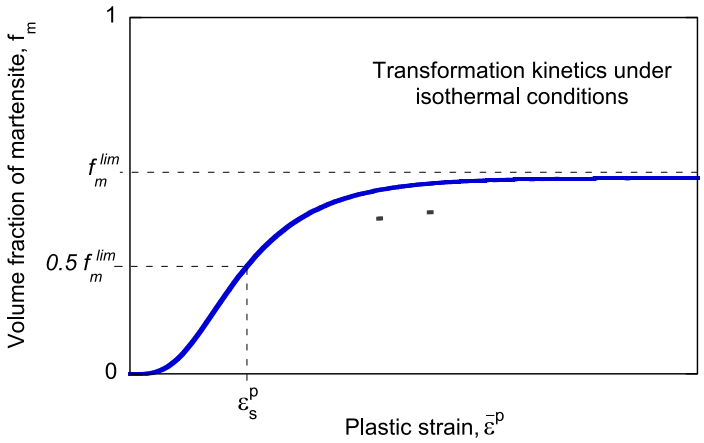

Fig. 10. f_m^{lim} and $\varepsilon_s{}^p$ as parameters controlling the kinetics of martensitic transformation under isothermal conditions. Both are defined through material parameters α_0 in Eq. (4) and g_0 in Eq. (8).

Previous analysis leads to the following conclusion: at sufficiently high loading rates, when inertia effects have complete control on the necking strain, the role of adiabatic heating in reducing the flow stress improves the material ductility.

Fig. 9 shows the dimensionless specific energy absorbed by SIMT and SIMTT material behaviors upon a wide range of initial strain rates $1\ s^{-1} \le \dot{\varepsilon}_0 \le 5 \times 10^5\ s^{-1}$. One should note that for any loading rate computed, the dimensionless specific energy absorbed by the SIMT is larger than that calculated for the SIMTT. Furthermore, the gap between both material models increases with the loading rate. Regarding the SIMTT material, the beneficial effect of having greater ductility than the SIMT at high loading rates does not balance the detrimental effect of having smaller flow stress.

Previous analysis leads to the following conclusion: at sufficiently high loading rates, when inertia effects have complete control on the necking strain, the better performance is provided by the material displaying larger flow stress if energy absorption needs to be maximized.

7. The role played by the transformation kinetics in necking inception and energy absorption capacity

Under quasi-static conditions both ductility and energy absorption are intrinsically linked to the amount of austenite present in the undeformed steel (e.g. in a multiphase TRIP steel) and by the stability of this phase. Under dynamic conditions, as previously shown, ductility and energy absorption are also influenced by inertia. Additionally, in adiabatic conditions the strong temperature increase expected due to both plastic dissipation and latent heat may affect SIMT.

Next, the influence of the transformation kinetics on ductility and energy absorption under dynamic conditions is studied. Different kinetics have been considered, controlled by two parameters (Fig. 10): the maximum fraction of transformed martensite f_m^{lim} and the value of plastic deformation at half-transformation ε_s^p (corresponding to $f_m = 0.5 f_m^{lim}$). The first one is linked to the value of the flow stress once the transformation is finished. For a given value of f_m^{lim}, the second parameter is linked to the rate of transformation hardening. Both parameters are defined for a constant temperature deformation process ($T = T_0$), since the transformation kinetics is commonly evaluated in quasi-static conditions for engineering purposes.

We start examining the role played by ε_s^p and f_m^{lim} on the process of necking inception, paying attention to three selected cases (Fig. 11a):

- Case I: $\varepsilon_s^p = 0.2$ and $f_m^{lim} = 30\%$. This will be considered the reference case.
- Case II: $\varepsilon_s^p = 0.2$ and $f_m^{lim} = 70\%$. In comparison with case I, here the fraction of martensite at saturation is drastically increased. This boosts the transformation hardening. The saturation flow stress strongly increases and the plastic strain at which the transformation ends is slightly delayed.
- Case III: $\varepsilon_s^p = 0.5$ and $f_m^{lim} = 70\%$. In comparison with case II, here the plastic strain at half-transformation increases. The plastic strain at which the transformation ends is strongly delayed, decreasing the slope of the stress–strain curve. Notice that cases II and III have the same saturation flow stress.

It is worth to mention that the kinetics of transformation, and therefore the stress–strain curves, are strongly modified if the deformation process is dynamic and approaches adiabaticity. Fig. 11b shows the flow stress upon deformation for the three cases considered in the analysis. Since temperature stabilizes the austenite, the stress strongly decreases. Moreover for the same value of f_m^{lim}, cases II and III, a larger value of the strain at half-transformation ε_s^p leads to a decrease of the saturation flow stress. Transformation in case III takes place over a larger range of plastic strains than in case II and, therefore, at higher temperatures that stabilize austenite and hinder martensite nucleation. This strengthens the idea that, at high rates of deformation, the choice of a steel grade showing SIMT should not rely on transformation curves obtained in quasi-static conditions, since the kinetics of transformation markedly changes due to thermal effects.

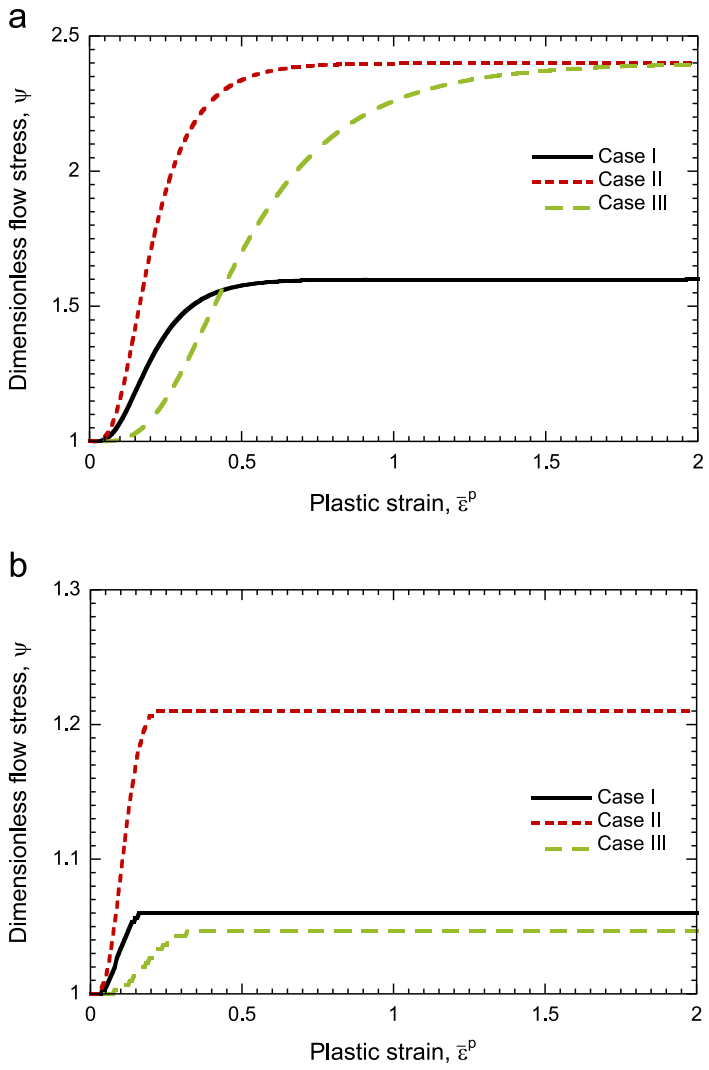

Fig. 11. Dimensionless flow stress versus equivalent plastic strain for case I ($\varepsilon_s = 0.2, f_m^{lim} = 70\%$) $f_m^{lim} = 30\%$), case II ($\varepsilon_s = 0.2, f_m^{lim} = 70\%$) and case III ($\varepsilon_s = 0.5$, in (a) quasi-static (isothermal) conditions, (b) dynamic (adiabatic) conditions.

7.1. Stability analysis results

Next, the results obtained from the stability analysis are discussed. Here, it is important to highlight the relation between dominant wavenumber, given by the stability analysis, and necking pattern, which will be obtained from finite element simulations. Fig. 12 illustrates the dimensionless dominant wavenumber versus strain at perturbation for cases I, II and III in adiabatic conditions. It is important to point out that, since the constitutive equation is strain rate independent, the dominant wavenumber does not depend on the loading rate. For the sake of clarity, the relation $\overline{\xi}_c$–ε_1 is analyzed for the three cases separately:

- Case I: the perturbation grows for any value of plastic strain considered. At the onset of straining the dominant wavenumber decreases due to the enhancing effect of the martensitic transformation on the material strain hardening. Approximately for $\varepsilon_1 = 0.05$ the dominant wavenumber reaches a minimum which coincides with the maximum slope in the stress–strain curve of the material. Larger plastic strains lead to a continuous increase of the dominant wavenumber.
- Case II: the perturbation does not grow for the whole range of plastic strains considered. At the onset of the deformation process the dominant wavenumber markedly decreases due to the severe transformation hardening displayed by the material. At a certain plastic strain $\varepsilon_1 \sim 0.05$ the dominant wavenumber goes to zero and the plastic flow becomes stable. The range of material stability extends until $\varepsilon_1 \sim 0.10$. From this point on the perturbation grows again and, at $\varepsilon_1 \sim 0.20$, the dominant wavenumber calculated for case II intersects that determined for case I. Then, the values of $\overline{\xi}_c$ calculated for cases I and II coincide for any plastic deformation.
- Case III: the perturbation grows for any value of strain at perturbation considered. For $\varepsilon_1 \lesssim 0.20$, the dominant wavenumber keeps largely constant. Within this range of plastic strains the wavenumber decrease induced by the transformation hardening is balanced by the wavenumber increase yielded by the plastic strain development. For plastic strains larger than 0.25 the values of $\overline{\xi}_c$ calculated for cases I, II and III coincide for any plastic deformation.

Fig. 13 shows the dimensionless critical perturbation growth $\overline{\eta}_c^+$ versus strain at perturbation ε_1 for cases I, II and III. Although the results shown in Fig. 13 are calculated for $\dot{\varepsilon}_0 = 15\,000\ \mathrm{s}^{-1}$, note that the discussion conducted below applies for any loading rate. Variations in the loading rate would change the values but neither the general trends nor the relation between cases I, II and III.

- Case I: the trend for the critical perturbation growth is similar to that found for the critical wavenumber. At the onset of the deformation $\overline{\eta}_c^+$ decreases up to $\varepsilon_1 = 0.05$ due to the emerging transformation hardening, and then continuously increases with ε_1.
- Case II: the critical perturbation growth markedly decreases at the onset of the deformation process due to the strong strain hardening, going to zero at $\varepsilon_1 \sim 0.05$. At $\varepsilon_1 \sim 0.10$ the plastic flow becomes unstable. Based on the results shown in Fig. 13, it is expected that, if necking develops for low values of strain, case II will show larger ductility than case I. Likewise, the trend will be inverted if necking develops for large values of strain.
- Case III: for $\varepsilon_1 \lesssim 0.20$, the critical perturbation growth keeps largely constant, with larger values than those corresponding to cases I and II. Then, the curve $\overline{\eta}_c^+$–ε_1 calculated for case III is intersected and exceeded by the curves calculated for cases I and II, in that order. Based on the results shown in Fig. 13, it is expected that case III will show the lowest ductility if necking develops for low values of strain, and the largest one if necking develops for large values of strain.

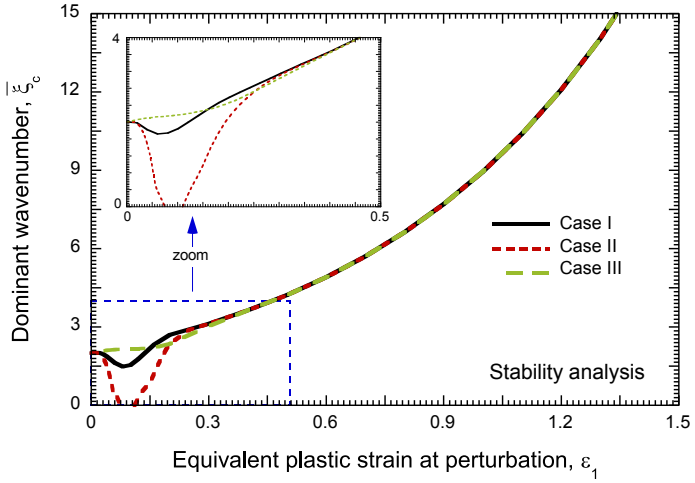

Fig. 12. Dominant wavenumber versus equivalent plastic strain at perturbation for case I ($\varepsilon_s^p = 0.2$, $f_m^{lim} = 30\%$), case II ($\varepsilon_s^p = 0.2$, $f_m^{lim} = 70\%$) and case III ($\varepsilon_s^p = 0.5$, $f_m^{lim} = 70\%$) in dynamic (adiabatic) conditions. Values are strain rate independent. Results from linear stability analysis.

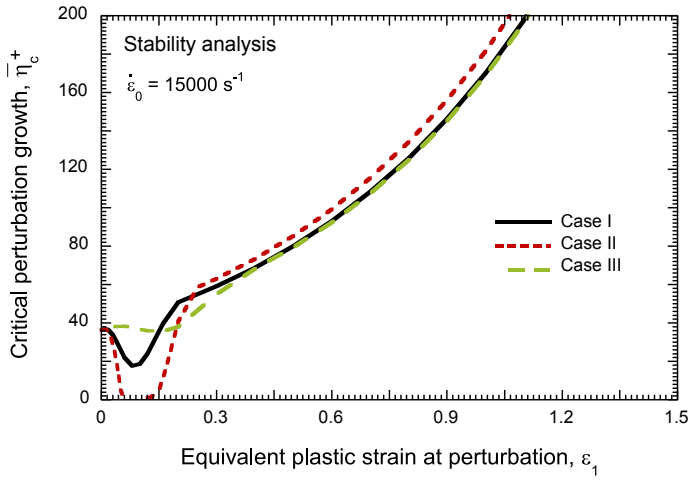

Fig. 13. Critical perturbation growth versus equivalent plastic strain at perturbation for case I ($\varepsilon_s^p = 0.2, f_m^{lim} = 30\%$), case II ($\varepsilon_s^p = 0.2, f_m^{lim} = 70\%$) and case III ($\varepsilon_s^p = 0.5, f_m^{lim} = 70\%$) in dynamic (adiabatic) conditions and at $\dot{\varepsilon}_0 = 15\,000\ s^{-1}$. Results from linear stability analysis.

Next, results of the finite element computations are presented and explained based on previous analysis.

7.2. Finite element analysis results

An additional analysis of cases I, II and III was conducted with the finite element model. The results confirm the observations found with the linear stability analysis. Fig. 14 shows the necking pattern corresponding to a low value of the strain rate, 5000 s^{-1}. Cases I and III develop the same number of necks whereas case II develops a lower number. Note that the number of necks is not proportional to the necking strain; according to the perturbation analysis, at low strain rates the instability develops at low values of the plastic strain. And, as illustrated in Fig. 12, in this range of strains the dominant wavenumber is similar for cases I and III and lower for case II, in full agreement with the finite element results. Fig. 15 shows the necking pattern corresponding to a high value of $\dot{\varepsilon}_0$ (40 000 s^{-1}): the number of necks incepted in the bar increases with the strain rate. At high strain rates the number of necks is proportional to the necking strain for all cases: the instability develops at large values of the plastic strain, and therefore the number of necks is dictated by the necking strain. These results confirm that, when inertia controls the loading process, the inception of necks is a deterministic process, rather than a random one. This conclusion is consistent with the observations reported by the authors (Rodríguez-Martínez et al., 2013c).

Regarding the ductility of the three different reference materials considered for this study, at low strain rates case II shows the largest and case III the lowest, as shown in Fig. 14. At high strain rates, on the contrary, case III shows the largest ductility and case II the lowest, as reported in Fig. 15. This observation fully agrees with the previous analysis of the results shown in Fig. 13.

Ductility and energy absorption are core factors in the selection of a steel for crashworthiness or impact applications. Based on the previous analyses, a detailed study of the influence of transformation kinetics on these two variables at low and high strain rates will be next presented. The ranges of the maximum fraction of transformed martensite and of the value of plastic deformation at half-transformation considered in this analysis have been widened in order to encompass a greater spectrum of grades showing SIMT: 10–90% in intervals of 20% for f_m^{lim}, and 0.10–0.50 in intervals of 0.05 for ε_s^p.

Ductility follows the same trends pointed out by the linear stability analysis, as shown in Fig. 16: at low necking strains (corresponding to a lower value of strain rate, 5000 s^{-1}) ductility increases with increasing f_m^{lim}, whereas at large necking strains (corresponding to a greater value of strain rate, 40 000 s^{-1}) ductility decreases with increasing f_m^{lim}. Therefore at high strain rates, a grade with a higher value of transformed martensite at saturation may be less ductile. Regarding the influence of ε_s^p, the strain rate also changes the trends: at low strain rates (5000 s^{-1}), values of ε_s^p above 0.3 promote a decrease in ductility, whereas at high strain rates (40 000 s^{-1}) larger values of ε_s^p always increase the ductility. This observation was also confirmed by the linear stability analysis (see definition of cases I, II and III).

The strain rate modifies the effect of transformation kinetics in the energy absorption capability. As Fig. 17 shows, for applications in which the strain rate is in the order of 5000 s^{-1}, values of ε_s^p below 0.2 promote a decrease in the energy absorbed by the steel (lower ductility due to a quick stabilization of the flow stress at a high value), and values of ε_s^p above 0.3 may also lead to a decrease in the energy (lower ductility and, additionally, lower value of flow stress). Intermediate values of ε_s^p (around 0.20–0.30 for this analysis) seems to bring an optimal value in terms of energy absorption. At higher strain rates in the order of 40 000 s^{-1}, a fast transformation will favor the energy absorption. In any case, it is clear that a large amount of metastable austenite in the undeformed state – and thus a larger value of f_m^{lim} – is always favorable for energy absorption.

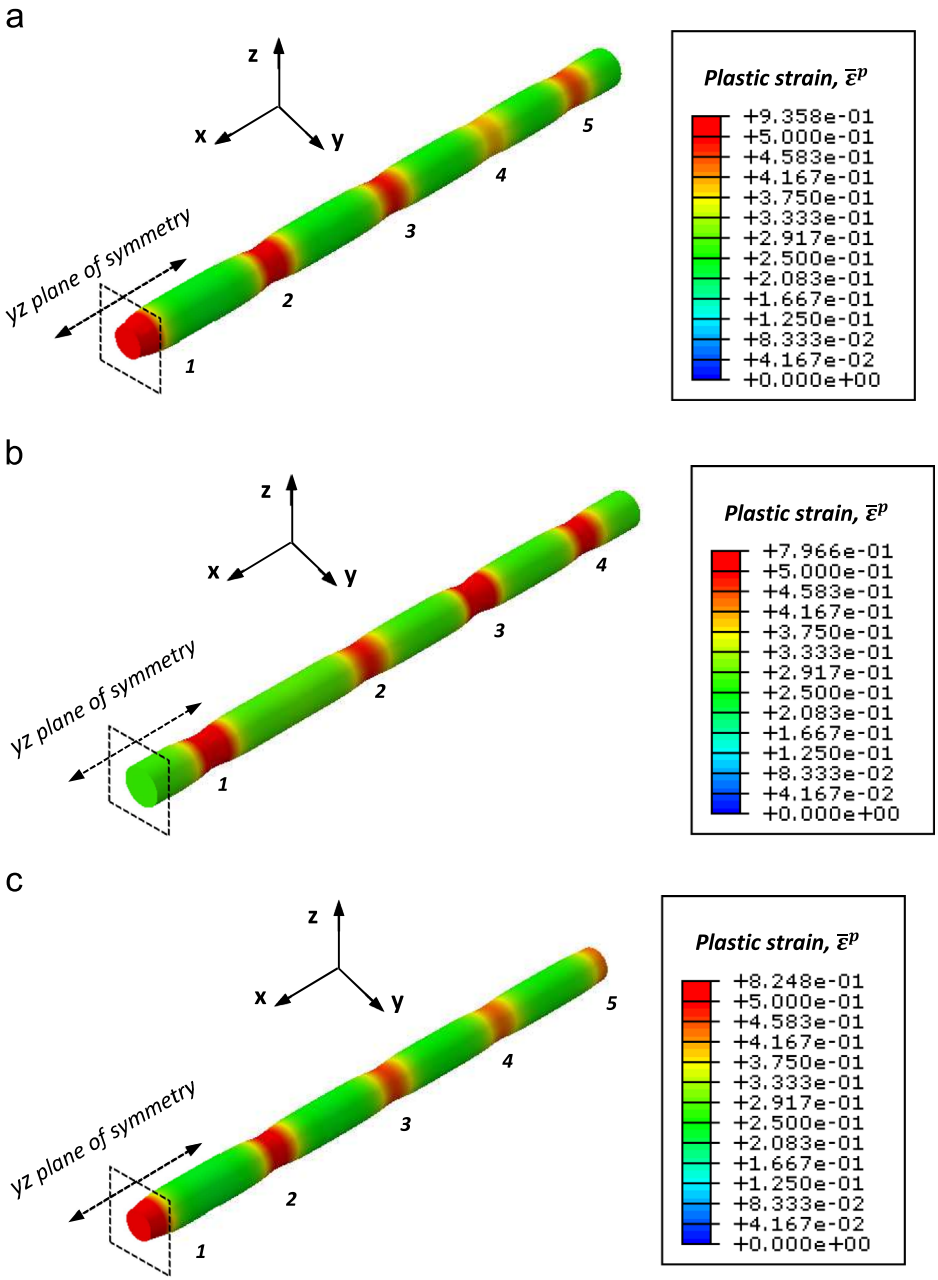

Fig. 14. Necking pattern in dynamic (adiabatic) conditions for SIMT material at $\dot{\varepsilon}_0 = 5000\ s^{-1}$ in (a) case I ($\varepsilon_s^p = 0.2$, $f_m^{lim} = 30\%$), (b) case II ($\varepsilon_s^p = 0.2$, $f_m^{lim} = 70\%$), (c) case III ($\varepsilon_s^p = 0.5$, $f_m^{lim} = 70\%$). Results from finite element calculations. (a) Case I: Loading time, $t = 76\ \mu s$ – Localized necking strain, $\bar{\varepsilon}^p_{neck} = 0.222$, (b) Case II: Loading time, $t = 84\ \mu s$ – Localized necking strain, $\bar{\varepsilon}^p_{neck} = 0.272$ and (c) Case III: Loading time, $t = 74\ \mu s$ – Localized necking strain, $\bar{\varepsilon}^p_{neck} = 0.213$.

From this analysis, the following conclusion arises: the choice of an optimal transformation kinetics which provides both maximum ductility and energy absorption capacity is attainable at low strain rates, whereas at high strain rates both goals are opposed and the selection should point out to one *or* the other.

8. Concluding remarks

The dynamics of multiple neck formation in high rate extension of materials exhibiting strain induced martensitic transformation have been investigated. For that task two different methodologies have been developed: (1) a linear stability technique derived within a quasi-1D theoretical framework, specifically developed to account for SIMT; (2) finite element simulations of slender bars subjected to uniaxial tension using a specific constitutive equation to consider SIMT. The finite element computations, together with the stability analysis results, permit to draw the following main conclusions:

- At sufficiently high strain rates (on the order of $10^4\ s^{-1}$ for the conditions considered in this work), when inertia controls the loading process, the martensitic transformation may not improve the ductility of the material nor its capacity for

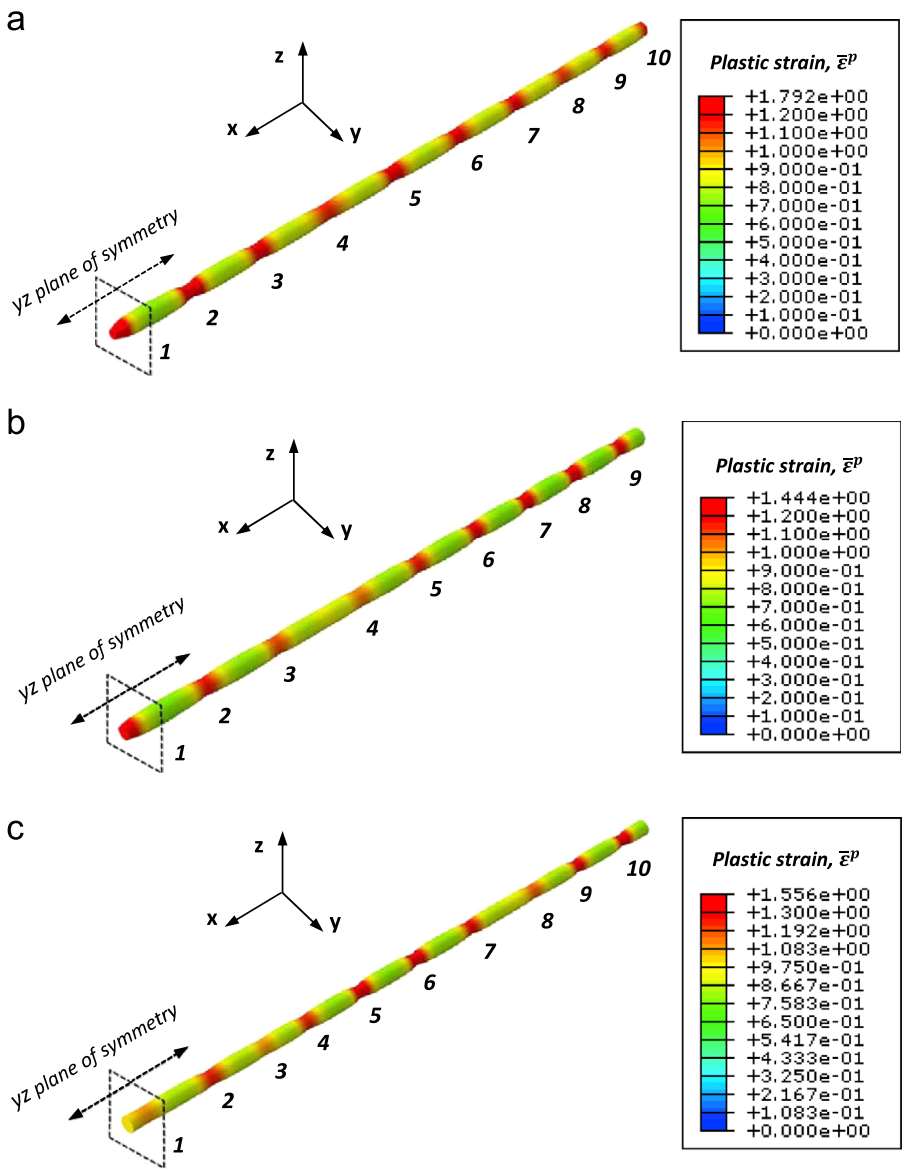

Fig. 15. Necking pattern in dynamic (adiabatic) conditions for SIMT material at $\dot{\varepsilon}_0 = 40\,000\ \mathrm{s}^{-1}$ in (a) case I ($\varepsilon_s^p = 0.2$, $f_m^{lim} = 30\%$), (b) case II ($\varepsilon_s^p = 0.2$, $f_m^{lim} = 70\%$), (c) case III ($\varepsilon_s^p = 0.5$, $f_m^{lim} = 70\%$). Results from finite element calculations. (a) Case I: Loading time, $t = 40.5\ \mu\mathrm{s}$ – Localized necking strain, $\bar{\varepsilon}^p_{\mathrm{neck}} = 0.814$, (b) Case II: Loading time, $t = 36.5\ \mu\mathrm{s}$ – Localized necking strain, $\bar{\varepsilon}^p_{\mathrm{neck}} = 0.753$ and (c) Case III: Loading time, $t = 43.0\ \mu\mathrm{s}$ – Localized necking strain, $\bar{\varepsilon}^p_{\mathrm{neck}} = 0.852$.

energy absorption. This behavior, barely reported in the literature from the authors' knowledge, indicates that the use of this type of materials in very high loading rate applications may need additional assessment.

- In case of deformation under adiabatic conditions, the temperature rise slows down the martensitic transformation which reduces the transformation hardening. On one hand, this decreases the capacity of the material for energy absorption but, on the other, it enhances the material ductility at high strain rates. Therefore, the temperature increase may not contribute to plastic localization.
- Material ductility and energy absorption capacity are usually considered as proportional or even tied together. However our observations clearly show that they are different concepts that, under certain loading conditions and material behaviors, show different – and sometimes opposite – dependences on yield stress, strain hardening and temperature sensitivity of the material. In the design of metallic components and structures potentially subjected to high loading rates (on the order of $10^4\ \mathrm{s}^{-1}$ for the conditions considered in this research) is necessary to identify whether ductility or energy absorption capacity is required.
- However, in materials exhibiting SIMT it is possible to achieve an efficient compromise solution between ductility and energy absorption capacity controlling the kinetics of the transformation (and therefore the flow stress and transformation hardening of the material). One should note that such possibility only applies within ranges of strain rate for which inertia does not control the loading process.

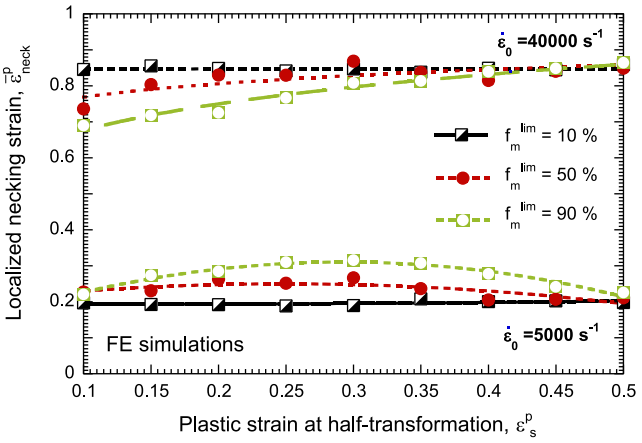

Fig. 16. Localized necking strain at $\dot{\varepsilon}_0 = 5000\ s^{-1}$ and $\dot{\varepsilon}_0 = 40\,000\ s^{-1}$ for various values of f_m^{lim} and ε_s^p. Results from finite element simulations.

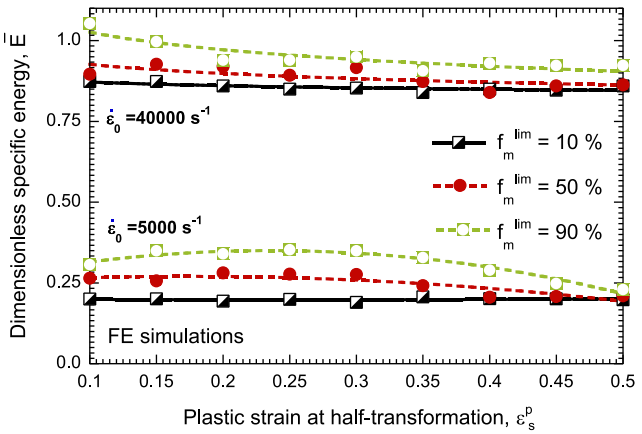

Fig. 17. Specific energy at $\dot{\varepsilon}_0 = 5000\ s^{-1}$ and $\dot{\varepsilon}_0 = 40\,000\ s^{-1}$ for various values of f_m^{lim} and ε_s^p. Results from finite element simulations.

The selection of steels showing SIMT for energy absorption in crash, blast or impact applications, requires a particular analysis in which the transformation kinetics at high strain rates should be thoroughly considered. In this work, the authors pointed out the specific models needed to develop the above analysis.

Acknowledgments

The authors are indebted to the Ministerio de Ciencia e Innovación de España (Projects DPI/2011-24068 and DPI/2011-23191) for the financial support.

The authors express sincere gratitude to Professor Alain Molinari for helpful discussions on multiple necking problems, and to Professor Daniel Rittel for helpful discussions on thermomechanical coupling in dynamically phase transforming metals.

References

Altynova, M., Hu, X., Daehn, G.S., 1996. Increased ductility in high velocity electromagnetic ring expansion. Metall. Trans. A 27, 1837–1844.
Andersson, R., 2005. Deformation Characteristics of Stainless Steels (Ph.D. thesis). Lulea University of Technology, Sweden.
Beese, A., Mohr, D., 2011. Effect of stress triaxiality and Lode angle on the kinetics of strain-induced austenite-to-martensite transformation. Acta Mater. 59, 2589–2600.
Beese, A., Mohr, D., 2012. Anisotropic plasticity model coupled with Lode angle dependent strain-induced transformation kinetics law. J. Mech. Phys. Solids 60, 1922–1940.
Bleck, W., Larour, P., Bäumer, A., 2005. High strain rate tensile testing of modern car body steels. Mater. Forum 29, 21–28.
Bridgman, P.W., 1952. Studies in large plastic flow and fracture, with special emphasis on the effects of hydrostatic pressure. In: Scientific Papers, Mechanics of Solids, vol. 1. McGraw-Hill Book Company, Inc., New York, pp. 9–37.
Considère, A.G., 1885. L'emploi du fer de l'acier dans les constructions. Ann. Ponts Chaussées 9, 574–575.

Dan, W.J., Li, S.H., Zhang, W.G., Lin, Z.Q., 2008. The effect of strain-induced martensitic transformation on mechanical properties of TRIP steel. Mater. Des. 29, 604–612.
Dean, J., Dunleavy, C., Brown, P., Clyne, T., 2006. Energy absorption during projectile perforation of thin steel plates and the kinetic energy of ejected fragments. Int. J. Impact Eng. 36, 1250–1258.
Doghri, I., 2000. Mechanics of Deformable Solids: Linear and Nonlinear, Analytical and Computational Aspects. Springer, Berlin.
Dudzinski, D., Molinari, A., 1991. Perturbation analysis of thermoviscoplastic instabilities in biaxial loading. Int. J. Solids Struct. 27, 601–628.
Fressengeas, C., Molinari, A., 1985. Inertia and thermal effects on the localization of plastic flow. Acta Metall. 33, 387–396.
Fressengeas, C., Molinari, A., 1994. Fragmentation of rapidly stretching sheets. Eur. J. Mech. A/Solids 13, 251–268.
Ghosh, A., 1977. Tensile instability and necking in materials with strain hardening and strain-rate hardening. Acta Metall. 25, 1413–1424.
Grady, D.E., Benson, D.A., 1983. Fragmentation of metal rings by electromagnetic loading. Exp. Mech. 12, 393–400.
Han, J.B., Tvergaard, V., 1995. Effect of inertia on the necking behaviour of ring specimens under rapid axial expansion. Eur. J. Mech. A/Solids 14, 287–307.
Hetherington, J., 1996. Energy and momentum changes during ballistic perforation. Int. J. Impact Eng. 18, 319–337.
Hill, R., 1958. A general theory of uniqueness and stability in elastic–plastic solids. J. Mech. Phys. Solids 6, 236–249.
Hu, X., Daehn, G.S., 1996. Effect of velocity on flow localization in tension. Acta Mater. 44, 1021–1033.
Jones, N., 1997. Structural Impact. Cambridge University Press, Cambridge.
Jones, N., Abramowicz, W., Belytschko, T., Ambrosio, J., Wismans, J., Viano, D., 2001. Crashworthiness: Energy Management and Occupant Protection. CISM Series. Springer.
Jovic, C., Wagner, D., Herve, P., Gary, G., Lazzarotto, L., 2006. Mechanical behaviour and temperature measurement during dynamic deformation on split Hopkinson bar of 304L stainless steel and 5754 aluminium alloy. J. Phys. IV 134, 1279–1285.
Knoche, P., Needleman, A., 1993. The effect of size on the ductility of dynamically loaded tensile bars. Eur. J. Mech. A/Solids 12, 586–601.
Langdon, G.S., Schleyer, G.K., 2005. Inelastic deformation and failure of profiled stainless steel blast wall panels. Part I. Experimental investigations. Int. J. Impact Eng. 31, 341–369.
Langdon, G.S., Schleyer, G.K., 2006. Deformation and failure of profiled stainless steel blast wall panels. Part III. Finite element simulations and overall summary. Int. J. Impact Eng. 32, 988–1012.
Lichtenfeld, J.A., Mataya, M., Tyne, C.J.V., 2006. Effect of strain rate on stress–strain behavior of alloy 309 and 304L austenitic stainless steel. Metall. Mater. Trans. A 37A, 147–161.
Lu, G., Yu, T., 2003. Energy Absorption of Structures and Materials. Woodhead Publishing, Cambridge.
Mercier, S., Molinari, A., 2003. Predictions of bifurcations and instabilities during dynamic extensions. Int. J. Solids Struct. 40, 1995–2016.
Mercier, S., Molinari, A., 2004. Analysis of multiple necking in rings under rapid radial expansion. Int. J. Impact Eng. 30, 403–419.
Needleman, A., 1991. The effect of material inertia on neck development. In: Yang, W.H. (Ed.), Topics in Plasticity. AM Press, Ann Arbor, MI, pp. 151–160.
Oliver, S., Jones, T.B., Foularis, G., 2007. Dual phase versus TRIP strip steels: microstructural changes as a consequence of quasi-static and dynamic tensile testing. Mater. Charact. 58, 390–400.
Olson, G., Cohen, M., 1975. Kinetics of strain-induced martensitic nucleation. Metall. Trans. A 6A, 791–795.
Papatriantafillou, I., Agoras, M., Aravas, N., Haidemenopoulos, G., 2006. Constitutive modeling and finite element methods for TRIP steels. Comput. Methods Appl. Mech. Eng. 195, 5094–5114.
Regazzoni, G., Montheillet, F., 1985. High strain rate ductility in uniaxial tension: a review. J. Phys. Tome 46, C5–435.
Rittel, D., Ravichandran, G., Venkert, A., 2006. The mechanical response of pure iron at high strain rates under dominant shear. Mater. Sci. Eng. A 432, 191–201.
Rodríguez-Martínez, J.A., Pesci, R., Rusinek, A., 2011. Experimental study on the martensitic transformation in AISI 304 steel sheets subjected to tension under wide ranges of strain rate at room temperature. Mater. Sci. Eng. A 528, 5974–5982.
Rodríguez-Martínez, J.A., Rittel, D., Zaera, R., Osovski, S., 2013a. Finite element analysis of AISI 304 steel sheets subjected to dynamic tension: the effects of martensitic transformation and plastic strain development on flow localization. Int. J. Impact Eng. 53, 206–216.
Rodríguez-Martínez, J.A., Rusinek, A., Pesci, R., Zaera, R., 2012. Experimental and numerical analysis of the martensitic transformation in AISI 304 steel sheets subjected to perforation by conical and hemispherical projectiles. Int. J. Solids Struct. 50, 339–351.
Rodríguez-Martínez, J.A., Vadillo, G., Fernández-Sáez, J., Molinari, A., 2013b. Identification of the critical wavelength responsible for the fragmentation of ductile rings expanding at very high strain rates. J. Mech. Phys. Solids 61, 1357–1376.
Rodríguez-Martínez, J.A., Vadillo, G., Zaera, R., Fernández-Sáez, J., 2013c. On the complete extinction of selected imperfection wavelengths in dynamically expanded ductile rings. Mech. Mater. 60, 107–120.
Rubin, M.B., Rodríguez-Martínez, J.A., 2013. The effect of radial inertia on flow localization in ductile rods subjected to dynamic extension. Int. J. Impact Eng., submitted for publication.
Rusinek, A., Klepaczko, J.R., 2009. Experiments on heat generated during plastic deformation and stored energy for TRIP steels. Mater. Des. 30, 35–48.
Rusinek, A., Zaera, R., 2007. Finite element simulation of steel ring fragmentation under radial expansion. Int. J. Impact Eng. 34, 799–822.
Rusinek, A., Zaera, R., Forquin, P., Klepaczko, J.R., 2008. Effect of plastic deformation and boundary conditions combined with elastic wave propagation on the collapse site of a crash box. Thin-Walled Struct. 46, 1143–1163.
Sato, K., Inazumi, T., Yoshitake, A., Liu, S., 2013. Effect of material properties of advanced high strength steels on bending crash performance of hat-shaped structure. Int. J. Impact Eng. 54, 1–10.
Shenoy, V.B., Freund, L.B., 1999. Necking bifurcations during high strain rate extension. J. Mech. Phys. Solids 47, 2209–2233.
Simó, J.C., Hughes, T.J.R., 1998. Computational Inelasticity. Springer, New York.
Simulia, 2013. ABAQUS/Explicit User's Manual, version 6.11 Edition. Dassault Systèmes, Providence, USA.
Sørensen, N.J., Freund, L.B., 1998. Dynamic bifurcation during high-rate planar extension of a thin rectangular block. Eur. J. Mech. A/Solids 17, 709–724.
Stringfellow, R.G., Parks, D.M., Olson, G.B., 1992. A constitutive model for transformation plasticity accompanying strain-induced martensitic transformations in metastable austenitic steels. Acta Metall. Mater. 40 (7), 1703–1716.
Tomita, Y., Iwamoto, T., 1995. Constitutive modelling of TRIP steel and its application to the improvement of mechanical properties. Int. J. Mech. Sci. 37, 1295–1305.
Triantafyllidis, N., Waldenmyer, J.R., 2004. Onset of necking in electro-magnetically formed rings. J. Mech. Phys. Solids 52, 2127–2148.
Vadillo, G., Rodríguez-Martínez, J.A., Fernández-Sáez, J., 2012. On the interplay between strain rate and strain rate sensitivity on flow localization in the dynamic expansion of ductile rings. Int. J. Solids Struct. 49, 481–491.
Walsh, J.M., 1984. Plastic instability and particulation in stretching metals jets. J. Appl. Phys. 56, 1997–2006.
Xue, Z., Vaziri, A., Hutchinson, J., 2008. Material aspects of dynamic neck retardation. J. Mech. Phys. Solids 56, 93–113.
Zaera, R., Rodríguez-Martínez, J.A., Casado, A., Fernández-Sáez, J., Rusinek, A., Pesci, R., 2012. A constitutive model for analyzing martensite formation in austenitic steels deforming at high strain rates. Int. J. Plast. 29, 77–101.
Zaera, R., Rodríguez-Martínez, J.A., Rittel, D., 2013. On the Taylor–Quinney coefficient in dynamically phase transforming materials. Application to 304 stainless steel. Int. J. Plast. 40, 185–201.
Zhou, F., Molinari, J.F., Ramesh, K.T., 2006. An elasto-visco-plastic analysis of ductile expanding ring. Int. J. Impact Eng. 33, 880–891.